Yngve Grøstad

Fluid-Structure Interaction Study of Vortex-Induced Vibration in Thermowells

Master's thesis in Mechanical Engineering
Supervisor: Reidar Kristoffersen
June 2019

Master's thesis

NTNU
Norwegian University of Science and Technology
Faculty of Engineering
Department of Energy and Process Engineering

NTNU
Norwegian University of
Science and Technology

DNV·GL

Yngve Grøstad

Fluid-Structure Interaction Study of Vortex-Induced Vibration in Thermowells

Master's thesis in Mechanical Engineering
Supervisor: Reidar Kristoffersen
June 2019

Norwegian University of Science and Technology
Faculty of Engineering
Department of Energy and Process Engineering

NTNU
Norwegian University of
Science and Technology

Preface

This report is the product of the masters project in TEP4925 - Engineering Fluid Mechanics, Master's Thesis. The study was conducted during the spring semester of the fifth and last year of my MSc in Mechanical Engineering at the Norwegian University of Science and Technology.

Trondheim 10. juni 2019

Yngve Grøstad

Acknowledgements

I would like to express my gratitude to my supervisor Associate Professor Reidar Kristoffersen for the valuable guidance given throughout the project, DNV-GL Noise & vibration advisory service for providing an interesting and challenging scope of the thesis. And the Department of Energy and Process Engineering at NTNU for providing computational resources for the simulations. Lastly, I would like to thank my colleague Ivar Gravdal for his help and input while proofreading the thesis.

Abstract

Thermowells are typically subjected to both static and dynamic forces due to the surrounding flow. The dynamic forces caused by vortex shedding can become problematic if locked-in with the natural frequency of the thermowell. When this happens, fatigue of the material and consequently cracking can occur due to the high stresses. As the location and magnitude of these stresses are unknown, an analysis of the vibratory characteristics and stresses caused by the fluid-structure interaction is therefore of interest.

This master's thesis presents the development of a fluid-structure interaction model for the case of a tapered thermowell subjected to a low density fluid flow. Firstly, the standalone fluid- and mechanical systems are presented before the coupling strategy are introduced. Results from both the standalone simulations are presented for model validation purposes before the FSI results are presented. The fluid flow is in the supercritical region and is modelled in ANSYS Fluent as a 3D RANS model using the Realizable $k - \varepsilon$ turbulence model with enhanced wall treatment. The structure, on the other hand, is modelled using ANSYS Mechanical as a transient 3D damped model.

The results from the FSI calculations show that the implementation of a one-way fluid-structure interaction model is adequate when simulating vortex-induced vibrations with low density ratios. The one-way model was able to capture cross-flow resonance of the thermowell and show that good results can be obtained at significantly cheaper computational cost with the use of a relatively cheap turbulence model and a one-way interaction model. Compared to similar studies with more demanding modelling, a reduction in runtime from 6-8 weeks to 6-8 days was obtained. Further, the tapering was found to be an effective way to suppress the resonant response of the structure. However, in resonance, the results conclude that the thermowell will still be exposed to fatigue due to the vibrations based on industrial criterions.

Sammendrag

Termolommer er typisk utsatt for både statiske og dynamiske belastninger grunnet strømningen rundt den. De dynamiske kreftene som kommer fra virvelavløsningen kan bli problematiske dersom de har samme frekvens som egenfrekvensen til termolommen. Når dette hender kan utmatting av materialet og eventuelt sprekkdannelser oppstå på grunn av de høye spenningene. Ettersom plasseringen og størrelsen av disse spenningene er ukjente ønskes en analyse av vibrasjonskarakteristikken og spenningene forårsaket av fluid-struktur interaksjonen av interesse.

Denne masteroppgaven presenterer utviklingen av en fluid-struktur interaksjonsmodell for en konisk termolomme under strømningsforhold med et lavt tetthets fluid. Først presenteres de frittstående fluid og struktur systemene før sammenkoblingen introduseres. Resultater for begge de frittstående simuleringene blir presentert for å validere modellene, før resultatene fra FSI simuleringene blir presentert og diskutert. Fluid systemet er modellert i ANSYS Fluent som en 3D transient RANS modell. Strømningens turbulens blir modellert ved bruk av en Realizable $k - \varepsilon$ turbulens-modell med *enhanced wall treatment*. Det strukturelle systemet blir modellert i ANSYS Mechanical som en 3D transient modell med dempning.

Resultatene fra FSI beregningene viser at en en-veis FSI modell er tilstrekkelig for å simulere vibrasjoner forårsaket av virvelavløsning ved lage tetthetsforhold mellom fluid og struktur. En-veis modellen var i stand til å fange opp kryss-strømningsresonans i termolommen og viser at gode resultater kan oppnåes selv ved bruk av mindre komplekse modeller. Sammenlignet med mer komplekse modeller fra litteraturen ble en reduksjon i kjøretid fra en CPU-tid på 6-8 uker til 6-8 dager oppnådd. Effekten av den koniske geometrien til termolommen med hensyn på resonans ble observert til å være et effektivt mottiltak for å unngå ekstrem resonans av strukturen. Likevel, basert på industrielle standarder viser resultatene at termolommen vil være utsatt for utmatting under resonante forhold.

Contents

List of Figures

List of Tables

Nomenclature

ρ_s	Structural density
u_s	Nodal displacement vector
$\dot{u}_s$	Nodal velocity vector
$\ddot{u}_s$	Nodal acceleration vector
$\mathbf{C}$	Structural damping matrix
$\mathbf{K}$	Structural stiffness matrix
$\mathbf{M}$	Structural mass matrix
$\mathbf{F}(t)$	Structural load vector
α	Mass-Matrix Damping Multiplier
β	Stiffness-Matrix Damping Multiplier
σ_e	von Mises stress
ζ	Damping ratio
f_n	Natural frequency
f_v	Vortex shedding frequency
V_r	Reduced velocity
St	Strouhal number

Abbreviations

CFD - Computational Fluid Dynamics
CSD - Computational Structural Dynamics
FIV - Flow-Induced Vibrations
FSI - Fluid-Structure Interaction
VIV - Vortex-Induced Vibrations

1 Introduction

"Fluid-structure interaction (FSI) is an interdisciplinary subject of interest to many researchers in the field of fluid dynamics."[38] The interaction is present in numerous examples, from trees in the wind to sediment erosion in the nature, to the aeroelasticity of airplanes and offshore structures in engineering systems.

Among the applications of fluid-structure interaction is the phenomena of flow-induced vibrations (FIV). Flow-induced vibrations have in recent decades become more and more important to engineers in a variety of industries. If left unattended in the structural design the phenomena can potentially cause catastrophic failures to structural systems as seen in the famous Tacoma Narrows Bridge collapse in 1940. In addition, unwanted noise pollution from high-frequency vibrations can be damaging to both the environment and human health and safety. FIV is closely associated with turbulence in the fluid which arises due to various flow-altering elements such as valves, bends, splits or instruments disrupting the flow. In industrial processes, the phenomena of FIV can pose a significant risk to the integrity and HSE of the assets.

1.1 Motivation

Thermowells are conical or straight hollow metal cylinders that are generally mounted inside large pipelines used for transport of various liquids and gasses. Inside the thermowells temperature sensors are mounted to measure the temperature in the pipe stream. Thus the sensor itself is protected from the potentially damaging fluid it measures. Though many variants of thermowells exist, in industrial applications the thermowell is most commonly based on a flanged design bolted onto a small-bore connection on the pipe. Thereby pointed into the stream.

The thermowells are typically subjected to both static and dynamic forces due to the surrounding flow. Most prominent and potentially damaging is the phenomena of vortex shedding on the thermowell. For certain flow rates in the pipe, the vortex shedding frequency can coincide with the natural frequency of the thermowell, potentially causing large vibrations and stresses in the thermowell due to the resonance phenomena. In several instances, cracking can occur at the base of the thermowell due to these stresses even though no high vibrations can be measured at the flange outside the pipe.

In recent years industrial companies have been troubled with issues linked to the fatigue of thermowell equipment. To prevent unnecessary maintenance and downtime of the process plants and ensure the integrity of the assets it is therefore of interest to better understand the physics behind the phenomena. Internal flow-induced motion is particularly difficult as it is harder to observe due to its enclosement as well as that experimental measurement tools can impact the motion and vibration in the system. Therefore it is of interest to investigate the possibility to use multi-physics software to study the problem. Although a selection of studies has been conducted by the use of a multi-physical approach before, they are often characterized by extremely high computational times. It is therefore of interest to investigate the use of a simpler FSI approach to see if reasonable results can be obtained at a cheaper cost.

1.2 Problem Description

This thesis is conducted at the request of DNV-GL Noise and Vibration advisory service to study the vortex-induced vibration (VIV) phenomena. The case is based on the vortex-induced vibrations of an industrial thermowell used in the oil & gas industry which has undergone some measurements and calculations by DNV-GL prior to this thesis. The thermowell that is to be investigated is of a flanged and tapered type. And the approach to this problem will be done with a fluid-structure interaction model, therefore the following tasks are to be considered:

1. Literature study of the flow around bluff bodies, vortex-induced vibrations and fluid-structure interaction.
2. Get familiarized with computational fluid dynamics and computational structural dynamics software.
3. Conduct numerical simulations with different levels of complexity.
4. Evaluate the results based on data from DNV-GL and/or simulations and experiments found in the literature.

1.3 Outline

Section 2 starts off with a quick review of available literature related to the thesis. In Section 3, background and theory for fluid dynamics, structural dynamics and fluid-structure interaction is presented. Section 4 covers the development of the FSI model. This including the development of the standalone fluid and structural models, as well as the coupling of the systems. In Section 5 the validation of the standalone systems are presented. Following this in Section 6 the results from the FSI simulations are presented and discussed. Lastly, Section 7 presents concluding remarks from the thesis and recommends further work and improvements.

2 Literature Review

Most research regarding fluid-structure interaction on flow-induced vibrations in the past has been related to marine and civil engineering issues such as; risers, offshore cables, mooring lines and buildings, and numerous methodologies have been presented with their accompanying advantages and disadvantages.

Early implementations of fluid-structure interaction as Herfjord et al. [17] research on vortex-induced vibrations of offshore structures in 1999 use a FEM-FEM coupling method. Showing good resemblance of the reality on flexible risers subjected to ocean currents. However, in recent years, the FEM-FEM approach has become more challenged by the FVM-FEM coupling used by most commercial softwares. Hofstede et al. [18] studied strong coupled FSI problems in nuclear reactor rods. Their study was conducted with both a $k - \omega$ SST and RSM turbulence models on FEM-FVM and FVM-FVM coupled systems, and it was found that for problems with a low density ratio between fluid and structure that the FEM-FVM coupling was 10 times more efficient compared to a FVM-FVM coupling.

Modern day FSI software has become increasingly robust and complex making it possible to model more and more demanding cases. This can be seen in De Nayer et al. [10] large eddy simulations of the flow past a cylinder with a flexible splitter plate in the subcritical region. Even with complex flow features and high deformations the computational expensive simulation produced frequencies with high accuracy. Utilizing a simpler model, Izhar et al. [20] studied a 2D, 2 degree of freedom case of the vortex-induced vibrations of a cylinder in cross-flow using the ANSYS CFX rigid body solver. The solver was able to recreate the phenomena with reasonable accuracy. Most research on the area are dominated by 2D simulations of vortex-induced vibrations, however with increasing Reynolds numbers 3D effects become more prominent. To account for 3D effects and tip-flow, Kinaci et al. [22] introduced a tip-flow correction factor when calculating VIV in cylinders with promising results. Using the System Coupling feature of ANSYS Workbench Raja [31] conducted his study on a horizontal cylindrical structure subjected to wave loads, thoroughly describing the implementation and methodology of the ANSYS' FSI software. It was shown that the dynamic amplification factor can deviate to a significant extent when using a one-way and a two-way coupling approach. This due to the fluid damping effect absent in the one-way approach. It should be noted that structural damping has been neglected in this case which could amplify this deviation.

Although flow-induced vibrations in cylindrical structures have become a more and more documented topic of interest over the years, flow around non-uniform cylinders can be said to have been paid less attention. Flow around tapered cylinders is a highly relevant case with regards to modelling heat exchangers, offshore structures and buildings. Parnaudeau et al. conducted a DNS of non-uniform cylinders, including tapered cylinders in uniform and shear flow [30]. The study showed a similar behaviour in the wake of a straight cylinder subjected to shear flow and a tapered cylinder subjected to uniform flow. The common features include cells of constant frequency, vortex dislocations and oblique shedding patterns. They suggested that the vortex dislocations may be responsible for the observed bending of the vortices towards a horizontal position. Similarly to Pernadeau's, Narasimhamurthy et al. [26] continued the research with a DNS of a tapered cylinder with a local Reynolds number of 300 and 102 at the wide and narrow end respectively. Surprisingly, similarities in the Reynolds averaged wake statistics between the tapered cylinder and straight cylinders was observed. With increasingly higher Reynolds number Hsiao et al. [19] found that the shedding frequency over a tapered with Reynolds numbers in the region $1 - 1.4 \cdot 10^4$ cylinder acts in a stepped manner as opposed to the constant shedding frequency of a straight cylinder as showed in Figure 1. It was furthermore found that for low values of Re, the transition from one shedding frequency to another can happen abruptly, while for higher values of Re the transition tend to be more smooth.

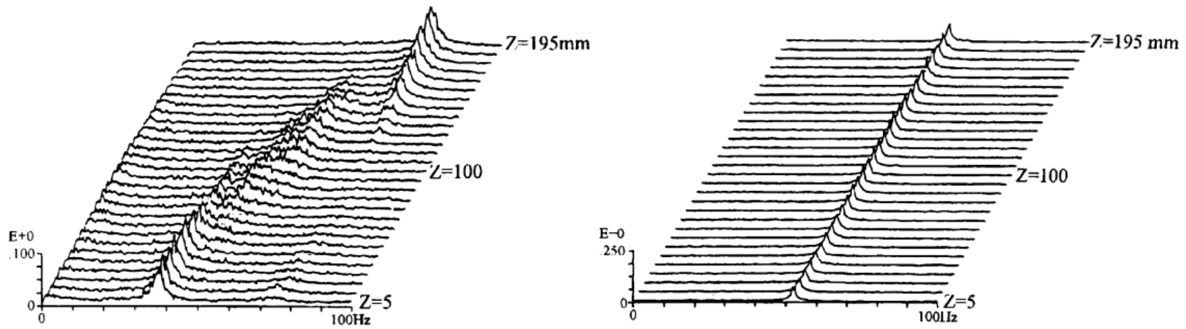

Figure 1: Power spectrum of the shedding frequency behind a: uniform cylinder; tapered cylinder. [19]

A study conducted by Litteaur et al. [25] show the effect of helical vortex suppressors on thermowells subjected to a high density methane gas flow in the supercritical regime. The study was conducted using a two-way interaction model with a Scale-Adaptive Simulation SST turbulence model, which can be said to be a hybrid model between a LES and RANS simulation [1]. Although not as computationally expensive as a LES model, using the SAS SST required 6-8 weeks of computational time in the FSI simulations.

3 Background

To be able to represent the system in a realistic manner numerous aspects of the physics at hand has to be considered. As mentioned prior, the problem deals with the interaction between fluid and structure and thus a combination of computational fluid dynamics (CFD) and computational structural mechanics (CSM) is to be used. It is therefore essential to understand the physical principles and governing equations of the system as well as the principles behind coupling the fluid and structural systems.

3.1 Vortex Shedding

In general fluid dynamics problems, it is common to describe their features by the Reynolds number. A dimensionless number describing the ratio of inertial to viscous forces based on the fluid velocity, viscosity and an appropriate length scale. In the case of a circular cylinder, the Reynolds number can be defined as

$$\mathrm{Re} = \frac{\mathrm{UD}}{\nu}$$

where U is the free stream velocity, D is the diameter of the cylinder and ν is the kinematic viscosity of the fluid.

When a uniform flow approaches the cylinder the fluid is brought to rest at a stagnation point at the front of the cylinder. Consequently causing a rapid increase in the pressure and initialization of a boundary layer over the face of the body. Increasing the flow velocity and thereby the Reynolds number causes the adverse pressure gradient behind the cylinder to become too large. When this happens the fluid momentum can no longer overpower the pressure gradient and the velocity gradient perpendicular to the surface eventually becomes zero, causing the flow to separate from the surface.

For Reynolds numbers above approximately 40, the wake of the body is destabilized causing oscillating velocity and pressure fluctuations to arise, commonly known as vortex shedding. The rate of which the vortex shedding occurs is called the vortex shedding frequency f_v and is commonly described by the non-dimensional Strouhal number

$$St = \frac{f_v D}{U} \tag{1}$$

relating the flow to the shedding frequency. The correlation between St and Re for a smooth and rough cylinder can be seen in Figure 2. Observe that for the majority of Reynolds numbers the Strouhal number has an approximately constant value of 0.2 with the exception of Reynolds numbers greater than 10^5. Different flow regimes are linked to the effects of different Reynolds numbers and turbulence. However, the regime of interest in this thesis is the supercritical region.

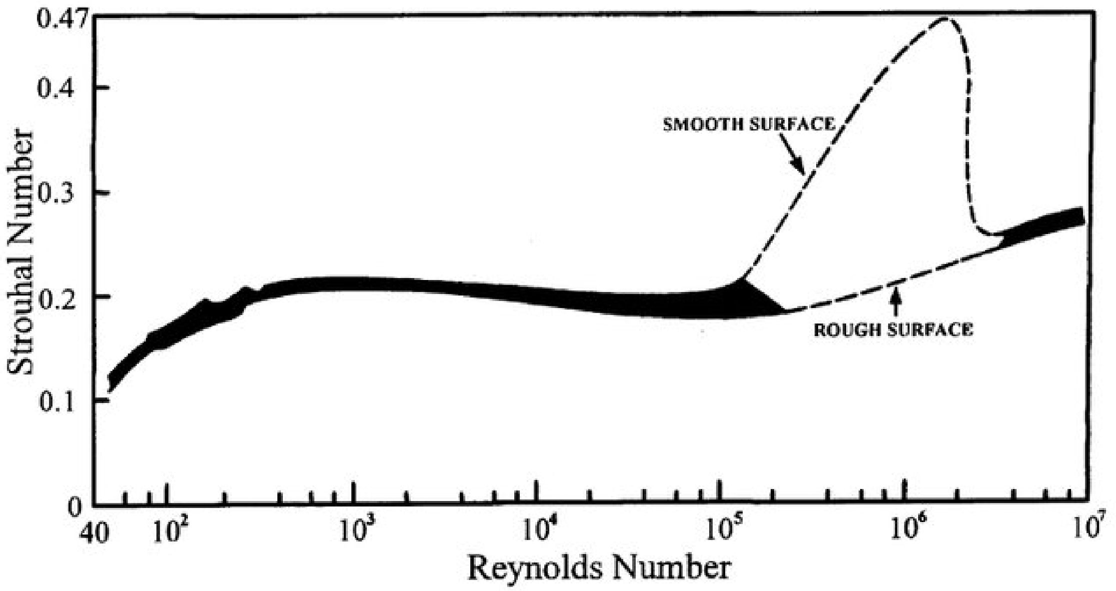

Figure 2: Relationship between Strouhal and Reynolds number [5].

As seen in Figure 2 a rapid increase in the Strouhal number occurs for Reynolds number in the order 10^5. This sudden increase in St around the supercritical region $3.5 \cdot 10^5 < Re < 1.5 \cdot 10^6$ is an effect of delayed boundary separation. In this region the boundary layers on both sides of the cylinder become turbulent at the separation point, thus the boundary layer separation is delayed due to the downward movement of the separation point. As the separation points are moved downstream the distance between them is also reduced consequently increasing the shedding rate.

3.2 Computational Fluid Dynamics

Computational fluid dynamics is a collection of numerical analyses used to solve and approximate problems containing for example fluid flow, heat transfer, multi-phase and chemical reactions. Numerous mathematical formulations based on for example the choice of discretization and physical modelling exists in the commercial and academic market today. However, in this thesis the commercial fluid solver ANSYS Fluent is used to solve the fluid flow which utilizes a finite volume method to solve the governing partial differential equations that define the problem.

3.2.1 Governing Equations

The flow around the tapered cylinder of the thermowell considered is assumed to be a incompressible, three-dimensional and turbulent case. Thus the flow is governed by the conservation of mass (2) and momentum (3).

$$\frac{\partial u_i}{\partial x_i} = 0 \tag{2}$$

$$\frac{\partial u_i}{\partial t} + \frac{\partial u_i u_j}{\partial x_j} = -\frac{\partial p}{\partial x_i} + \frac{1}{\mathrm{Re}} \frac{\partial^2 u_i}{\partial x_j \partial x_j} \tag{3}$$

Where x_i and x_j are spatial coordinates in the tensor notation and u_i and u_j is the corresponding velocity component.

3.2.2 Turbulence

In many situations it is not feasible or necessary to completely solve the Navier Stokes equations due to the extreme computational cost at higher Reynolds numbers. To reduce the computational cost a simplification of the Navier-Stokes equations based on time averaging the variables can be introduced. This is known as Reynolds Averaged Navier Stokes (RANS) and is obtained by decomposing the flow variables into mean $\bar{\phi}$ and fluctuating ϕ' parts as shown in equation (4).

$$\phi = \bar{\phi} + \phi' \tag{4}$$

By introducing the Reynolds decomposition (4) to the governing equations (2) and (3) and time-averaging the resulting equation yields the Reynolds Averaged Navier Stokes equation (5).

$$U_j \frac{\partial U_i}{\partial x_j} = \frac{1}{\rho} \frac{\partial}{\partial x_j} (-P\delta_{ij} + 2\mu S_{ij} - \overline{\rho u_i' u_j'}) \tag{5}$$

Where $S_{ij} = \frac{1}{2}(\frac{\partial U_i}{\partial x_j} + \frac{\partial U_j}{\partial x_i})$ is the mean strain rate, δ_{ij} is the Kroenecker delta function and $\overline{\rho u_i' u_j'}$ are the Reynolds stresses. These stresses introduce an additional 6 unknowns to be determined resulting in the well known closure problem of turbulence.

A common approximation to obtain closure of this problem is by usage of Boussinesq's eddy viscosity hypothesis relating the turbulence stresses to the mean flow:

$$-\overline{u_i' u_j'} = 2\nu_T S_{ij} - \frac{2}{3} k \delta_{ij} \tag{6}$$

Where k is the mean turbulent kinetic energy which is a measure of the turbulent intensity of the flow and is defined as:

$$k = \frac{1}{2}\overline{u_i' u_i'} \tag{7}$$

3.2.3 Realizable $k - \varepsilon$

By introducing the eddy viscosity hypothesis additional modelling is needed to solve the newly arose unknowns. The turbulence models based on the eddy hypothesis is the one-equation Spalart-Allmaras model as well as the more complex two-equation models k-ω and k-ε. As the problem of high Reynolds number flow around a circular cylinder includes both high adverse pressure gradients and separation the standard $k - \varepsilon$ model may not be applicable. However, the realizable $k - \varepsilon$ is considered to be applicable based on similar studies conducted and as: *"It is also likely to provide superior performance for flows involving rotation, boundary layers under strong adverse pressure gradients, separation, and recirculation."*[2] The transport equations for k and ε is given below:

$$\frac{\partial}{\partial t}(\rho k) + \frac{\partial}{\partial x_j}(\rho k u_j) = \frac{\partial}{\partial x_j}\left[\left(\mu + \frac{\mu_t}{\sigma_k}\right)\frac{\partial k}{\partial x_j}\right] + P_k + P_b - \rho\varepsilon - Y_M + S_k \tag{8}$$

$$\frac{\partial}{\partial t}(\rho\varepsilon) = \frac{\partial}{\partial x_j}\left[\left(\mu + \frac{\mu_t}{\sigma_\varepsilon}\right)\frac{\partial \varepsilon}{\partial x_j}\right] + \rho C_1 S_\varepsilon - \rho C_2 \frac{\varepsilon^2}{k + \sqrt{\nu\varepsilon}} + C_{1\varepsilon}\frac{\varepsilon}{k} C_{3\varepsilon} P_b + S_\varepsilon \tag{9}$$

The realizable $k - \varepsilon$ differs from the other $k - \varepsilon$ models in the way the eddy viscosity $\mu_t = \rho C_\mu k^2/\varepsilon$ is computed. As opposed to the other models, the realizable version does not assume a constant C_μ. It is modeled based on the mean strain and rotation rates, angular velocity of the system rotation and the turbulence fields. For a more detailed description of the turbulence model the reader is referred to the ANSYS manual [1].

3.2.4 Wall Treatment

When working with turbulent flows the problem of predicting the physics in the boundary layer near the wall is essential for obtaining accurate results. The boundary layer can be split up into 3 zones which can be mathematically described by their respective relationships between the dimensionless distance from the wall y^+ and a dimensionless velocity u^+, known as the inner variables. The 3 zones are often referred to as the viscous sublayer, the buffer zone and the fully turbulent logarithmic zone. The viscous sublayer, which is defined as the region $y^+ \leq 6$, is highly influenced by viscous stresses as a consequence of the large velocity gradients in this region. Here a linear relationship of $u^+ = y^+$ exists. The fully turbulent logarithmic zone is however mostly governed by the Reynolds stresses rather than viscous stresses as the velocity gradients become smaller. Here a logarithmic relationship between u^+ and y^+ exists at a form of $u^+ = A\text{log}(y^+) + B$, where A and B are constants determined by the flow. Lastly, between the viscous sublayer and the fully turbulent region the buffer zone is located. This is the most complex zone of the inner layer as neither viscous stresses nor Reynolds stresses are dominating.

To capture the flow features in the vicinity of a wall is computationally expensive as the complex flow features in the near wall region makes the computations dependent of a high-resolution mesh. To reduce the computational effort wall functions can be introduced, thereby modelling the viscosity affected region rather than resolving it. However, due to the expected flow separation in the cylinder region it is of interest to resolve the viscous sublayer. Thus the first cell needs to be located within the viscous sublayer, i.e. have a $y^+ < 5$. As the $k - \varepsilon$ model utilizes a standard wall function as default, which is only applicable for $30 < y^+ < 300$, the enhanced wall treatment option must be used in order to resolve the viscous boundary layer. Fluent's enhanced wall treatment combines enhanced wall functions with a two-layer wall treatment model. The mathematical details behind the enhanced wall treatment can be found in the Fluent Theory Guide [1]. When using the enhanced wall treatment function it is recommended that the first cell should at least be located within the viscous sublayer of $y^+ < 5$, however a $y^+ \approx 1$ is desired [2].

3.2.5 Forces

Due to the fluctuations of the vortex shedding, the pressure distribution along the cylinder will change periodically. Thus a periodic change in the forces acting on the cylinder will occur. The force components are divided into drag acting parallel to the free stream velocity and lift acting perpendicular to the free stream velocity.

Flow around bluff bodies is often characterized by the forces acting on the body. It is therefore necessary to define some characteristic properties related to the normal and tangential forces called the drag coefficient C_D and lift coefficient C_L.

$$\mathrm{C_D} = \frac{\mathrm{F_D}}{\frac{1}{2}\rho \mathrm{U}^2 \mathrm{A_{ref}}}$$

$$\mathrm{C_L} = \frac{\mathrm{F_L}}{\frac{1}{2}\rho \mathrm{U}^2 \mathrm{A_{ref}}}$$

Where F_D is the drag force, F_L is the lift force, ρ is the free stream density, U is the free stream velocity and A_{ref} is a characteristic reference area. In the case of flow around a straight or tapered cylinder, the projected area of the cylinder is used as the reference area. A typical relationship between the Reynolds number and mean drag coefficient and r.m.s. lift coefficient for flow around a circular cylinder is shown in Figure 3 and Figure 4.

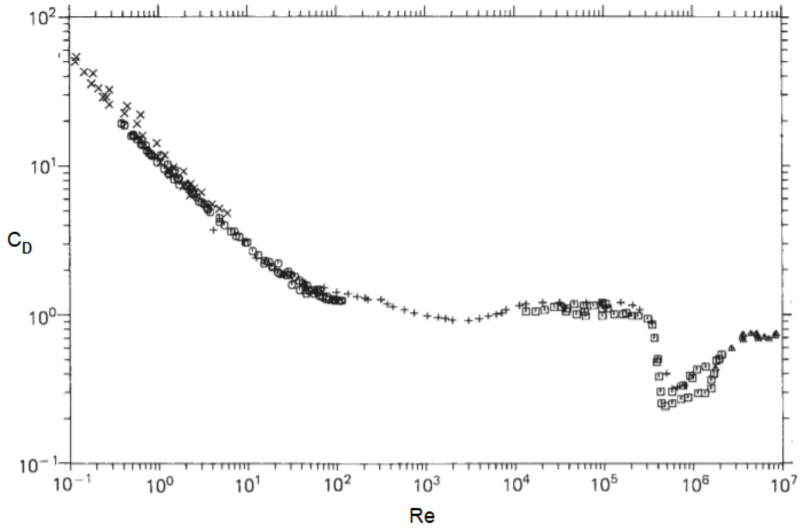

Figure 3: Mean drag coefficient as a function of the Reynolds number [29].

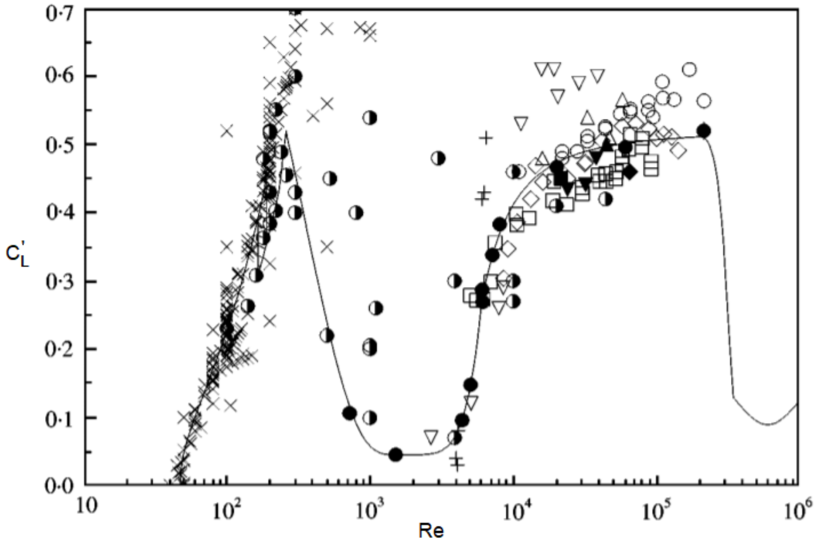

Figure 4: RMS values of the lift coefficient as a function of the Reynolds number [27].

3.3 Computational Structural Dynamics

The same methodology used in CFD can also be used to approximate problems in structural dynamics, thereby giving rise to the field of computational structural dynamics. In this thesis ANSYS Mechanical is used to solve the structural dynamics, which is a finite element based solver.

In this thesis, a thermowell subjected to oscillating forces is to be investigated and as a result of the applied forces, the thermowell will be subjected to vibrations. Vibrations is a result of the interaction between kinetic- and strain energy when a structural system is deformed [24]. As vibration is a time-dependent phenomena a dynamic analysis is therefore obviously suitable. Contrary to a static analysis, a dynamic analysis takes the inertia loads, or the structure's resistance to change in velocity and acceleration due to varying loads into account. The structural response of a system can be modelled as a mass-spring-damper system and by applying Newtons laws of motion, Lagrange–d'Alembert principle, virtual work and system equilibrium [24] the equation of motion can be formulated as (10).

$$m\ddot{u}_s + c\dot{u}_s + ku_s = F(t) \tag{10}$$

Generalized for a multi degree of freedom system the equation can be written as a system of equations as (11)

$$\mathbf{M}\ddot{u}_s + \mathbf{C}\dot{u}_s + \mathbf{K}u_s = \mathbf{F}(t) \tag{11}$$

where $\mathbf{M}$ is the structural mass matrix, $\mathbf{C}$ is the structural damping matrix, $\mathbf{K}$ is the structural stiffness matrix, $\ddot{u}_s$ is the nodal acceleration vector, $\dot{u}_s$ is the nodal velocity vector, u_s is the nodal displacement vector and $\mathbf{F}(t)$ is the structural load vector.

3.3.1 Finite Element Method

Solving the equation of motion given in equation (11) can be done with various approaches. However, the most frequently used is the Finite Element Method (FEM). This is a well established numerical technique used to conduct Finite Element Analysis (FEA) on physical problems. Similar to the finite volume method, FEM is used for obtaining approximate solutions to the partial differential equations, however FEM is usually to be preferred when dealing with structural analysis.

3.3.2 Material Properties

The material properties are a critical factor to the response in a structural analysis. For high stresses, material nonlinearities can become relevant if for example plastic deformation occurs. However, the structural analysis in this thesis will be subjected to low forces and thus small deformations. As a result of this, the stresses will not exceed the yield limit and thus be confined to the linear elastic region. Young's modulus is a material property measuring the stiffness of a solid in the linear elasticity region. It's defined as the ratio between stress and strain as $E = \sigma/\varepsilon$ where E is the Young's modulus, σ is the stress and ε is the strain. For steel alloys commonly used as the material for thermowells, the Young's modulus is usually in the region of 180 - 200 GPa.

Another important material property in structural analysis is Poisson's ratio which relates the materials tendency to expand perpendicular to compression. Assuming axial compression or stretching the ratio can be written as $\nu_s = d\varepsilon_{transverse}/d\varepsilon_{axial}$. For general steel alloys the Poisson ratio is usually in the range of $0.27 < \nu_s < 0.31$.

3.3.3 Modal Analysis

In general, a modal analysis is used to establish a structure's vibratory characteristics. A modal analysis is one of the more fundamental transient structural analysis methods and commonly used as a starting point for designing structures and building more detailed analyses. The motivation to conduct a modal analysis is to locate frequencies and corresponding shapes where the structure magnifies the reaction to an applied load. Thereby being able to predict and circumvent critical loads or conditions which are damaging to the structure. To find these frequencies and shapes a free, undamped vibration is applied to equation (11). Rewriting this as an eigenvalue problem an expression for the natural frequency is obtained:

$$(\mathbf{K} - \omega^2\mathbf{M})\phi = 0 \tag{12}$$

Where ω is a frequency vector and ϕ is the corresponding eigenvalue vector. If the alternating forces discussed in section 3.3.6 approach a frequency close to a natural frequency of the structure the shedding frequency can abruptly synchronize with the structure's natural frequency. Commonly known as lock-in or synchronization.

3.3.4 Damping

In a real system, structural vibrations will fade out with time. The dissipated energy of the structured is characterized by the structure's damping factor or damping ratio ζ defined as:

$$\zeta = \frac{\text{energy dissipated per cycle}}{4 \cdot \text{total energy of structure}} = \text{damping ratio}$$

When a structure is excited and starts to vibrate the vibration will be damped due to energy dissipation in the structure. This damping effect is generated due to fluid damping, internal material damping and structural damping. The fluid damping is related to drag and viscous dissipation. The internal material damping due to yielding, heating, electromagnetic currents and internal energy dissipation and the structural damping by friction, impact etc. Industrial thermowells today typically have damping factors in the range 0.0005-0.002 (0.05-0.2% of critical damping) [6].

The simplest and most commonly used method to model damping of a structure is the Rayleigh damping or classical damping (13). The model assumes a linear relationship between the damping matrix $\mathbf{C}$ and the mass and stiffness matrices $\mathbf{M}$ and $\mathbf{K}$.

$$\mathbf{C} = \alpha\mathbf{M} + \beta\mathbf{K} \tag{13}$$

Where α represents the mass damping and β represents the structural damping. Assuming that the mass damping term related to the frictional damping is negligible due to the high frequencies, as done in similar studies [35]. The coefficient β can thus be found by equation (14)

$$\zeta_i = \frac{\alpha}{2\omega_i} + \frac{\beta}{2}\omega_i \tag{14}$$

where ζ_i is the modal damping ratio and ω_i is the corresponding eigenfrequency of mode i. Note that ω_i is in the form of angular frequency. The modal damping factor ζ is based on Blevins' [6] experiments on similar structures in similar conditions. In this case the value of $\zeta = 0.001$ (0.1%) is used, thus giving a $\beta = 1.206 \cdot 10^{-6}$.

3.3.5 Stress

Evaluating the stress in a structure in three dimensions can be difficult. Therefore the principal stresses are often related to a single scalar value called the equivalent stress or von Mises stress in the following way:

$$\sigma_e = \left[\frac{(\sigma_1 - \sigma_2)^2 + (\sigma_2 - \sigma_3)^2 + (\sigma_3 - \sigma_1)^2}{2}\right]^{1/2} \tag{15}$$

This scalar is related to determining if a structure will yield or fracture and states if the stresses are equal or greater than the material yield strength, the structure will yield.

3.3.6 Flow-Induced Vibrations

A common dimensionless quantity used when working with flow-induced vibrations is the reduced velocity V_r which is defined as:

$$V_r = \frac{U}{f_i D} \tag{16}$$

Where U is the flow velocity, D is the cylinder diameter and f_i is the natural frequency of the i^{th} mode of the cylinder.

As mentioned prior a critical situation occurs when the vortex shedding frequency coincides with the natural frequency of the structure. As the in-line and cross-flow forces have different frequencies, different relations apply. From recommended practises given by

DNV [12] a relation between V_r and St is given describing the lock-in regions. For in-line vibrations, the region is given by:

$$\frac{0.3}{St} < V_r < \frac{0.65}{St} \tag{17}$$

While for cross-flow vibrations the region is given by

$$\frac{0.8}{St} < V_r < \frac{1.6}{St} \tag{18}$$

representing the range in which the vortex shedding frequency may coincide with the eigenfrequency of the structure. Similarly, Blevins states that strong interaction between the structure and vortex shedding is observed for reduced velocities between 2 and 8 [5]. The structural response of a varying vortex shedding frequency is shown in Figure 5. It can be observed that the amplitudes of the cross-flow vibrations is significantly higher than that of in-line vibrations. This is due to that the lift alternates between a positive and negative force, while the drag is unconditionally positive.

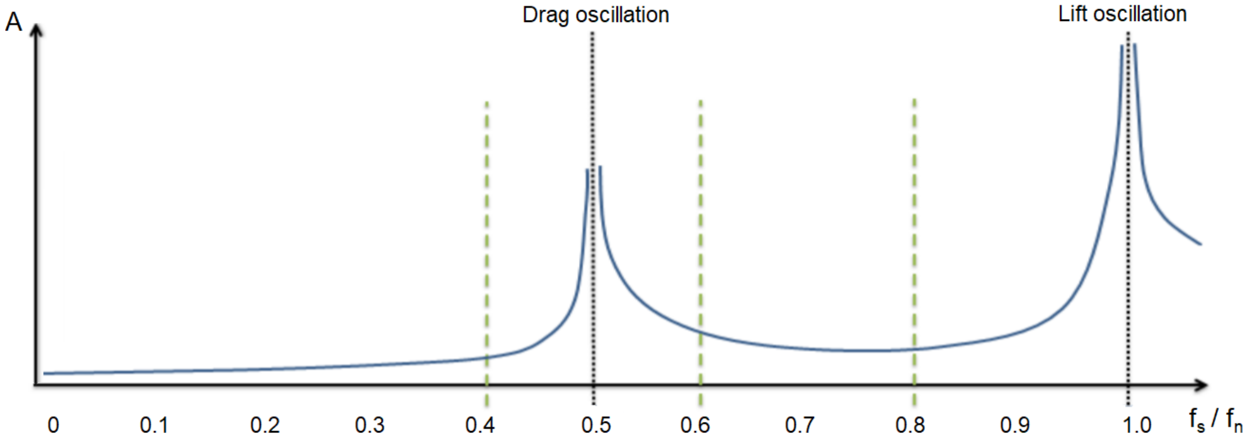

Figure 5: Amplitude frequency plot showing the different lock-in response of drag- and lift force oscillations.

3.4 Fluid-Structure Interaction

As this thesis is based on a fluid-structure interaction approach to vortex-induced vibrations, the CFD system and CSD system discussed in Section 3.2 and 3.3 have to communicate. Generally, multi-physical problems are inconvenient and hard to solve analytically due to their complexity. Thus a numerical or experimental approach is usually more favourable. Over the last decades, advanced commercial software and high computational power have made the numerical approach possible with high precision. Generally, numerical FSI calculations can be approached in two ways: monolithically or partitioned.

By usage of the monolithic system coupling approach, all systems are mathematically intertwined and solved as a single matrix system as seen in Figure 6. The interface between the coupled systems is treated synchronously, which opens up for conservation of properties at the interface thus, increasing the stability of the solution. However, according to Chimakurthi et al. [9] the monolithic approach generally result in ill-conditioned matrix systems as the different mathematical models have different stiffness leading to a possible loss of accuracy in the solution.

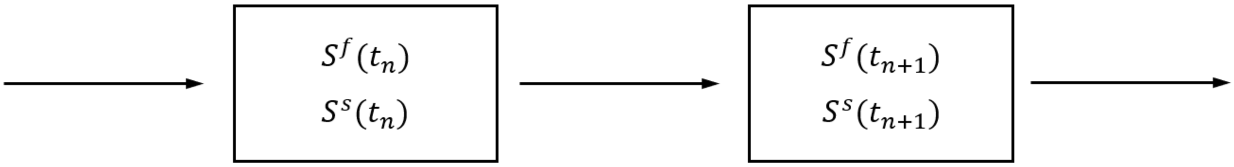

Figure 6: Monolithic fluid-structure interaction approach.

The monolithic approach is generally considered to the most robust approach to FSI, however it's highly computationally expensive and must be tailored to the specific problem and thereby most relevant for academic use.

The other approach to FSI is by the usage of a partitioned method. As opposed to the monolithic approach, the partitioned approach solves separate equations for the separate physical domains and a suitable coupling method is used to connect the interfaces. As indicated in Figure 7, the fluid and structural systems are solved in an alternating manner, in a defined sequence, using their respective solvers. The solution acquired from the fluid time-step is then used as a boundary condition for the structural solver and solved separately. Likewise, the displacement obtained from the structural solution is prescribed as a new boundary condition for the fluid solver. This process is repeated until a convergence criterion is met.

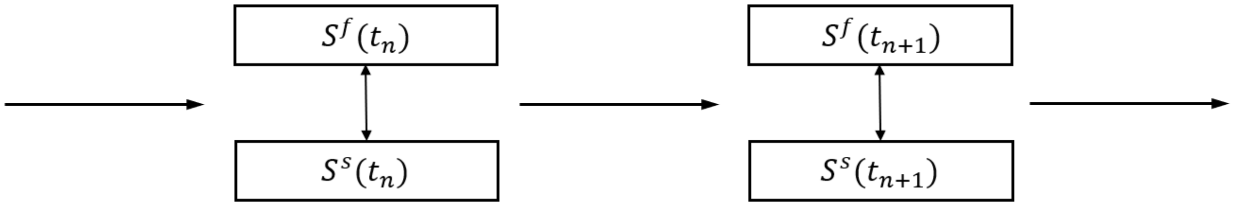

Figure 7: Partitioned fluid-structure interaction approach.

3.4.1 One-way Coupling

The simplest partitioned coupling model is achieved by coupling the systems in only one direction. This meaning that the flow exerts forces on the structure, but the reaction force and displacement of the structure is neglected in the fluid solver. This coupling method is of course highly more efficient than stronger coupling methods, but should only be used when the reaction of the structure on the fluid is of negligible importance. A flow chart of the one-way approach is shown in Figure 8.

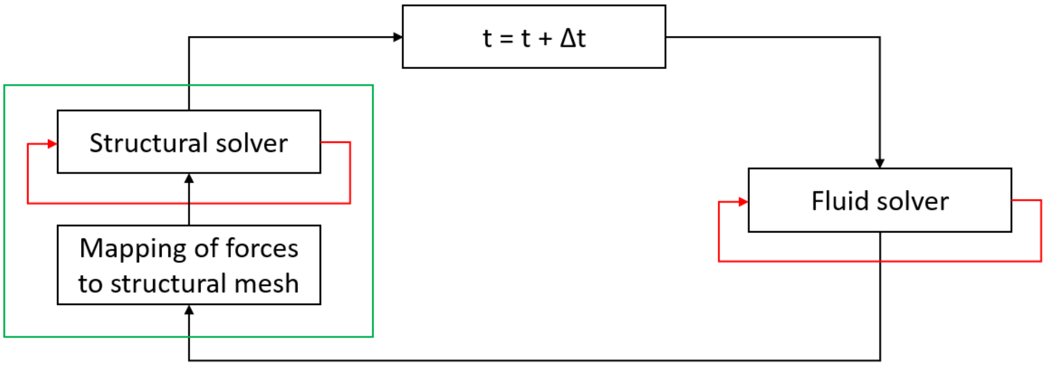

Figure 8: Flowchart of the one-way FSI coupling.

Initially, the fluid solver iterate until convergence is achieved for the given time-step. The calculated forces at the fluid-solid interface are then mapped onto the structural mesh before the transient structural solver is iterated until convergence.

3.4.2 Two-way Coupling

A stronger coupling can be achieved by using a two-way coupling scheme. For problems with a stronger connection between the systems, e.g. FSI with large deflections, a two-way coupling can represent the physics more accurately. The general algorithm of the two-way coupling is shown in Figure 9. Similarly to the one-way coupling, the solution from the fluid solver is mapped onto the structural mesh for a given time-step. However, the calculated displacements of the structure are sent back to the fluid solver which re-mesh the domain according to the given displacements. This iterative procedure is repeated until the change in forces and deflections has converged before proceeding to the next time-step.

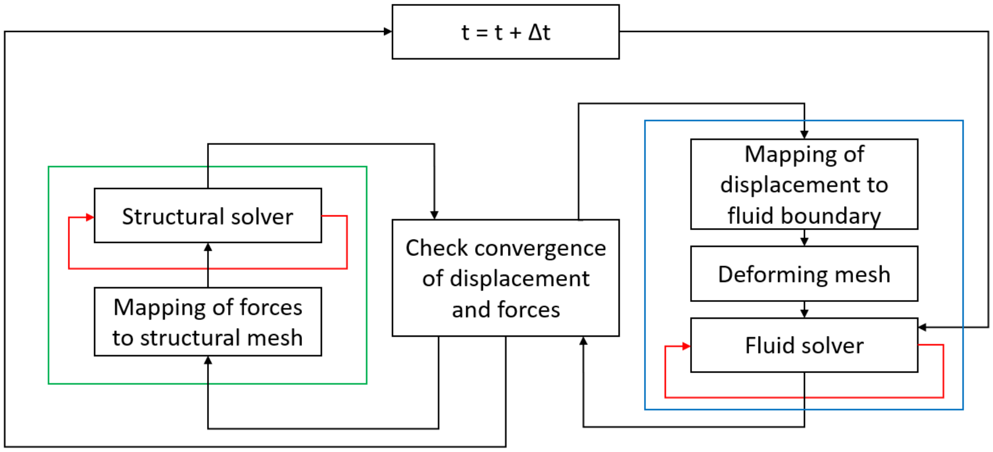

Figure 9: Flowchart of the two-way FSI coupling

3.4.3 System Coupling

In ANSYS, fluid-structure interaction simulations are conducted using the System Coupling component. System Coupling ties the individual Fluent and Mechanical participants together and once connected, System Coupling gathers information from each participant to synchronize the setup. This including general system information, coupling interface regions and variables such as forces and displacements connected to the coupling. Once Fluent and Mechanical is connected, the System Coupling component will be the governing system controlling the solver execution for both Fluent and Mechanical.

3.4.4 Data Transfer

When coupling the participating systems together they have to communicate. This is done by defining data transfer rules between the solvers. ANSYS' System Coupling currently supports the transfer of force, motion and thermal energy between systems.

ANSYS employs two data transfer algorithms depending on the variable to be transferred. For non-conserved quantities such as displacements and temperature, the profile preserving Smart Bucket algorithm is applied while for conserved quantities as mass and momentum the conservative profile preserving General Grid Interface algorithm is employed. It should be noted that when using the GGI algorithm, which is employed in the one-way interaction model, the sending participant Fluent should have a finer mesh than the receiving part. This to ensure that as much of the interface information as possible is sent.

4 Methodology

In accordance with ANSYS Best Practice Guidelines for using System Coupling, the different solvers are individually built up and validated prior to coupling the systems together [4]. Following this logic, the FSI model should therefore be valid if the coupling strategy used is appropriate.

A brief overview of the method used to solve the problem is given in this section. The section distinguishes between the methodology of the structural, fluid and fluid-structure interaction systems. ANSYS SpaceClaim is used to create the geometry in the model as shown in Figure 10, while both the finite volume and finite element mesh are created using ANSYS Meshing. Lastly, the two separate solvers are coupled in ANSYS Workbench using the System Coupling to execute the data transfer between the systems.

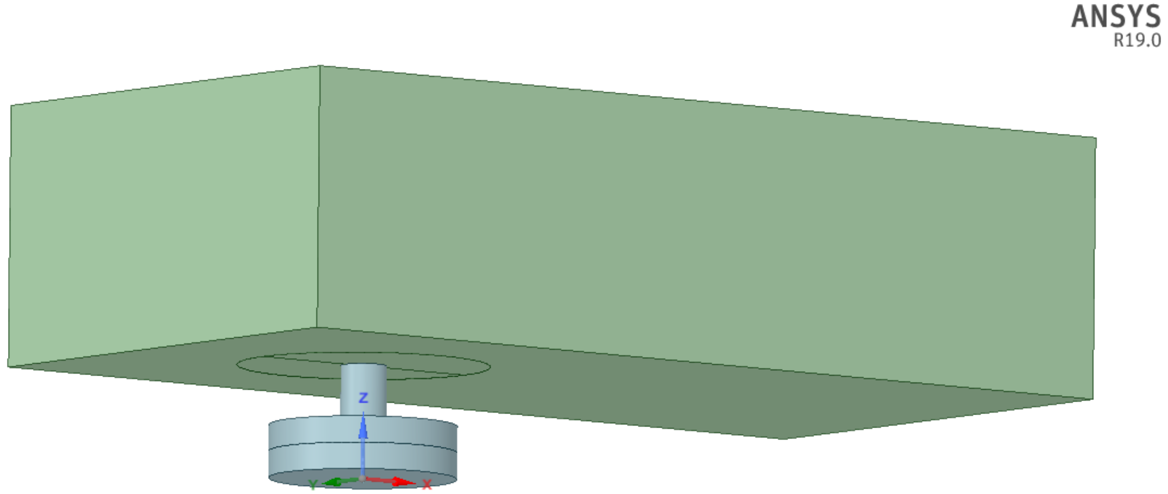

Figure 10: Assembled structural (grey) and fluid (green) geometry used in the FSI computations.

The standalone CFD simulations were carried out on the High-Performance Computing (HPC) cluster *IDUN* on NTNU's network. A maximum of 20 cores was found to reduce the computational time sufficiently for the largest cases. Due to the complexity of the system coupling of ANSYS Fluent and Mechanical, the use of the IDUN cluster is not possible even though HPC is supported by the application. Thus all FSI simulations have been performed locally on a medium-performance workstation with specifications of 64Gb RAM, i7-5820k 12 threaded 3.3GHz processor. Due to the relatively simple structural model, this was also validated locally.

4.1 Structural Model

The structural model is solved using the Transient Structural solver of ANSYS Mechanical APDL, which is a mechanical engineering tool to perform finite element analysis for structural analyses.

In this case, the structural model consists of a thermowell and a small-bore connection. The geometry of the thermowell component is shown in Figure 11a, and it can be seen here that the thermowell has a slight taper with a difference in root to tip diameter of 5mm. Thus yielding a taper ratio $l/(d_0 - d_1)$ of 58. The introduction of tapering to the thermowell is a common trick used when designing structures under fluid loads to break up the constant shedding frequency. The small-bore connection geometry is shown in Figure 11b. As seen, the small-bore has a relatively simple geometry consisting of a hollow cylinder with a thickness of 3.5mm with a flanged end.

It should be noted that as a simplification the connection of the two components is done by the use of a multi-point constraint formulation instead of a bolted connection which would be the case in real life.

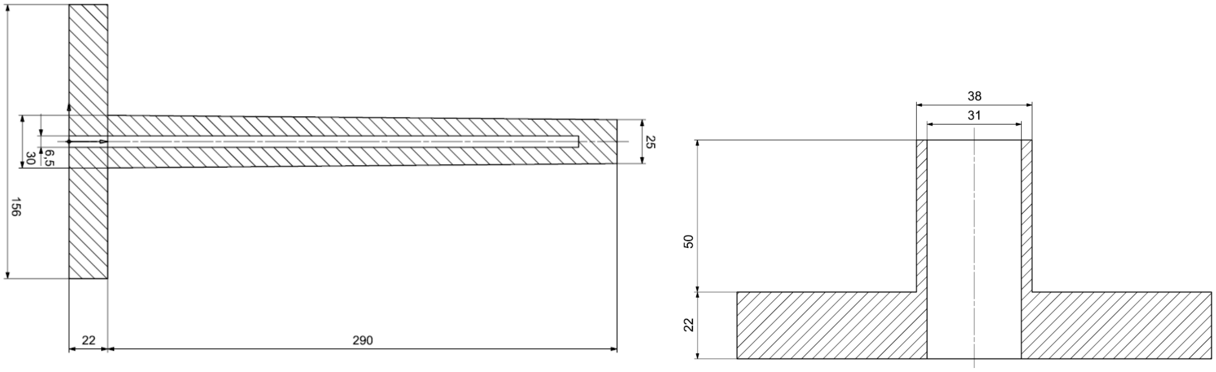

(a) Sectional draft of the flanged and tapered thermowell.

(b) Sectional draft of the small-bore connection.

Figure 11: Sectional draft drawings of the thermowell and small-bore system. Dimensions given in mm.

4.1.1 Material Properties

As a part of the preprocessing stage, the material properties of the structural components have to be defined. Due to the petrochemical fluids flowing in the pipe, both the thermowell and small-bore is composed of the austenitic Type 316 stainless steel, used to resist corrosion. It is assumed that the material has an isotropic elasticity where the bulk- and shear modulus is derived from Young's modulus and Poisson's ratio. Lastly, the Rayleigh damping control discussed in Section 3.3.4 has to be defined. This is done by adding the damping factor properties for α and β to the material. Where α-damping is introduced as a mass-matrix multiplier and β-damping as a stiffness-matrix multiplier. An overview of the specified material properties of the thermowell and small-bore connection are listed in Table 1.

Table 1: Material properties of the thermowell and small-bore components used in the simulations.

Property	Poisson's Ratio
Material	316 SS
Density [kg/m^3]	8000.0
Young's Modulus, E [GPa]	200.0
Poisson's Ratio, ν_s	0.30
Mass-Matrix Damping Multiplier	0
k-Matrix Damping Multiplier	$1.2058 \cdot 10^{-6}$

4.1.2 Mesh Generation

To achieve a high quality structural mesh of the thermowell it's important to assure that the physics are captured properly. Similar to the CFD mesh, the structural mesh has to produce a solution that is independent of the choice of mesh. However, the geometry of the thermowell and small-bore connection has a few features that complicates this process.

The sharp re-entrant corners seen in Figure 11, located between the cylindrical structures and the flange creates a stress singularity at which refining the mesh will increase the stress at the corner. As the theoretical stress at a singularity is infinitely large, convergence cannot be achieved when refining the mesh. By St. Venant's principle it could be argued that the model results outside of the contaminated regions are correct, however as the magnitudes of these stress concentrations are of interest, a fillet radius has been introduced to avoid the singularity. As no corner in a manufactured component can be perfectly sharp, this is generally considered to be a valid modelling technique used in finite element analysis today [8]. To ensure that the model resembles the real component as close as possible, a fillet radius of only 1.5mm was used in both components.

The ten node tetrahedral element Tet10, named SOLID187 in ANSYS Mechanical, was used for the structural meshing. This is a higher order 3D element with quadratic displacement behaviour. Each node in the element have three degrees of freedom, translation in x, y and z direction respectively [3]. The element sizing is determined using proximity sizing function and controlled locally at the filleted edges using face sizing to capture the stress concentrations properly. By using the techniques specified above, the mesh was created with an average mesh quality of 0.84 which is deemed sufficiently high to produce reliable results.

The generated thermowell and small-bore connection model and corresponding mesh can be seen in Figure 12a and Figure 12b.

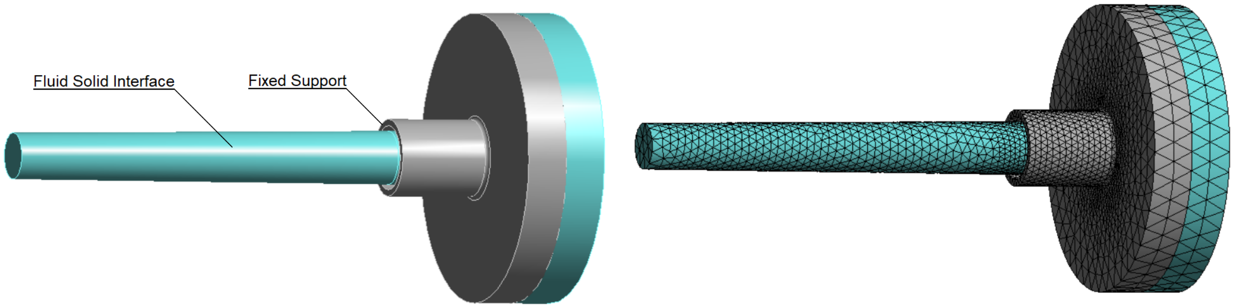

(a) Thermowell and small-bore connection geometry used for the meshing.

(b) Thermowell and small-bore connection structural mesh used in the finite element model.

Figure 12: Structural model from ANSYS Mechanical and the corresponding mesh from ANSYS Meshing.

To validate the mesh used in the finite element analyses, a varying force load in a similar order of magnitude as the forces expected from the CFD analysis was applied to the thermowell's Fluid-Solid Interface. This being magnitudes up to 50N.

4.1.3 Solution Setup

Prior to execution, boundary conditions and model properties of the structural system needs to be defined. The thermowell/small-bore system has a Fixed Support at the bottom, at the end of the small-bore connection as shown in Figure 12a. At the thermowell's cylinder surface, a Fluid Solid Interface is defined. This is done in order to be able to map the fluid forces from Fluent onto the structure in the FSI calculations. Due to the relatively low forces inflicted on the structure, the setting Large Deflections is turned off. When large deflections effects are turned off, a linear relationship between force and displacement is assumed. Thus the stiffness of the structure does not need to be recalculated at each time-step and a significant decrease in run-time is achieved.

Furthermore, the solver type used in the simulations is set to iterative, this because of its several advantages over the direct method. According to Ansys: "*the Iterative solver is preferred over the Direct solver for its efficiency in terms of solution time and memory usage.*"[3]

Lastly, the time-step and end time of the simulation has to be specified. For the mesh refinement study it was found that a time-step of $\Delta t = 0.0001$s was sufficiently small. In the FSI calculations, as the system coupling needs a consistent time-step between the CFD and CSD system, the time-step will be governed by Fluent due to the high Reynolds number.

4.1.4 Modal Analysis

To determine the modal response the model discussed in the prior subsections are imported into the standalone Modal Analysis system. Using the same mesh and fixed support, Mechanical only needs to be specified how many mode shapes which is to be calculated. The first 6 modes is calculated in this thesis.

4.2 Fluid dynamics

As very few numerical studies have been conducted on the flow around tapered cylinders in the supercritical region, the task of validating the model becomes harder than more scientifically popular problems. Therefore a systematic bottom-up strategy is used to approach the problem. First, a 2D model of a circular cylinder is simulated and validated to determine the appropriate selection of numerical modelling and computational mesh. These results are then used to determine appropriate meshing in a case with a straight cylinder with a diameter equal to the mean value of the tapered cylinder. Lastly, as the taper ratio of the thermowell is high and thereby closely similar to a straight cylinder, a 3D tapered cylinder case is created using the results obtained from the 3D straight cylinder case.

4.2.1 Mesh Setup

The computational domain for the validation cases is shown in Figure 13 and the corresponding geometric measures are listed in Table 2. Due to the absence of available data for validation the model is initially assumed to be in a rectangular domain rather than in a pipe. The domain size is based on similar studies conducted by Ong et. al [28] and it was found that this size was sufficient to suppress the unwanted influence of the boundaries.

A finer mesh in the vicinity of the cylinder is essential to achieve an accurate simulation due to the separation and vortex shedding occurring in this region. Thus the fluid mesh is split up into two bodies as shown in Figure 10. One containing the far-field domain and one the refinement region near the cylinder. This reduces the computational effort as the far-field regions can be meshed coarser than the volume around the cylinder, thus reducing the number of elements in the model. As the scope of this thesis is more focused on the forces acting on the cylinder rather than the wake, the wake region is omitted in the refinement. The refinement region is created as a secondary cylinder enclosing the structure with a diameter of 210mm ($7d_0$).

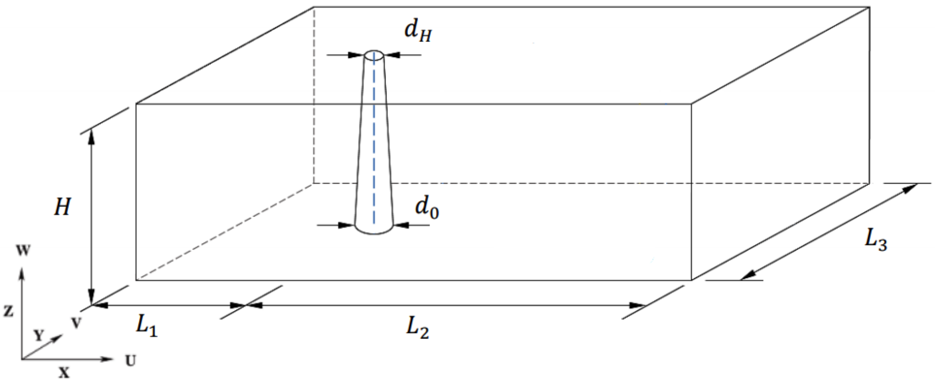

Figure 13: Computational domain of the Fluent system.

Table 2: Numerical values for the geometry of the computational fluid domain. Values given in mm.

d_0	d_H	H	L_1	L_2	L_3
30.0	25.0	290.0	210.0 ($7d_0$)	600.0 ($20d_0$)	420.0 ($14d_0$)

It should be noted that for the FSI cases d_0 and H is changed to 28.76mm and 218mm respectively. This due to the introduction of the small-bore connection which reduces the insertion length of the thermowell by 72mm.

Selecting an appropriate cell type is also a key factor concerning the results. In Fluent, generally tetrahedrons/hexahedrons or prism cells are recommended, however, pyramidal and polyhedral cells are also available. Due to the relatively simple geometry, a hexahedral mesh is used, reducing the cell count and thus computational cost significantly. It is also recommended to align the cells along the flow direction when possible to increase the accuracy, which is achieved more easily when using hexahedral cells. As this case has a prominent flow direction from the inlet to the outlet it also favours the use of hexahedral cells. In addition, hexahedral cells are to be favoured when predicting fluid forces as it has a tendency to produce higher accuracy [14].

Evaluating the quality of a mesh can be done in a variety of ways. A critical quality measure is the skewness, relating the cell corner angles to the optimum corner angles. For hexahedral celled meshes the optimal corners are perfectly perpendicular and deviations from this causes the line between adjacent cells to not pass through the face center. Causing inaccuracies in the calculations on cell faces. Highly skewed meshes are unacceptable and should have a value as close to 0 as possible even though a general rule of thumb states a criteria of 0.95 [2]. An average skewness of 0.0045 was obtained in the meshes, with a maximum skewness of 0.56 and is considered to be sufficiently good.

Further, if the cell face between two nodes is not orthogonal to both cells, the cell is defined as non-orthogonal. This affects the calculations as the line connecting the two adjacent cell-centers is not parallel to the face normal. This has a negative impact on the calculations of diffusive terms and is therefore of course unwanted. As a quality measure, the average orthogonal quality should be as close to 1 as possible, however the worst cell in the mesh should at least be larger than 0.01 [2]. An orthogonal quality of 0.995 was obtained in the meshes, with a minimum quality of 0.33 and is considered to be acceptable.

To obtain the desired near wall treatment described in Section 3.2.4, inflation layers are used on the face of the cylinder. The inflation layer consists of 20 layers with a first layer thickness of $1.5 \cdot 10^{-6}$m to ensure that the maximum y^+ value is below 5 over the entire span of the cylinder. The growth rate of the layer height is set to 1.25 to reduce the amount of layers needed while still capturing the necessary details near the wall. In addition, a growth rate of 1.25 was found to produce a smooth transition between the inflation zone and the surrounding mesh which is desirable.

Due to the fact that the enhanced wall treatment requires a very low first layer thickness near the wall, the aspect ratio at the innermost cells can become quite large. A maximum aspect ratio of 1800 is found at the innermost cells in the thin end of the cylinder. This is something that cannot be omitted when resolving the boundary layer of wall bounded turbulent flow. It should be noted that this constitutes a very small part of the total elements, where the average aspect ratio has a value of 80.

4.2.2 Boundary- and Initial Conditions

As the computational domain has to be finite, the model needs to have a collection of boundaries to surround the mesh. To be able to model the problem in a realistic manner, it is essential to prescribe appropriate boundary and initial conditions in the simulation. The selection of the boundary conditions in a simulation should be selected such that the solution is physical and represent the reality.

A generic fluid, representing a high density gas is used in the simulations to give a fluid/structure mass ratio of $\rho_f/\rho_s = 0.01$, i.e. $\rho_f = 80\text{kg/m}^3$. The dynamic viscosity of the fluid is therefore set to $\mu_f = 4.4 \cdot 10^{-5}\text{kg/ms}$, thus giving a inlet velocity of $U = 20\text{m/s}$ to obtain a Reynolds number of $\text{Re} = 10^6$ based on a cylinder diameter of 27.5 mm.

The boundaries confining the model is the inlet and outlet, the cylinder wall and the top, bottom and side walls of the domain. The prescribed conditions used for these boundaries are listed below.

- At the inlet, a uniform flow is specified with $u_1 = U$ and $u_2 = u_3 = 0$. The corresponding free stream turbulence is defined by the turbulent kinetic energy k and a turbulent length scale L/D. The free stream turbulent kinetic energy is based on a turbulent intensity I_u of 0.8% whilst L/D is set to 0.0045.
- At the outlet a pressure-outlet boundary condition is imposed.
- For viscous flow a fluid particle at a surface will have no velocity relative to the surface. Thus at the cylinder wall a no-slip boundary condition of $u_1 = u_2 = u_3 = 0$ is applied for all simulations in this thesis.
- A symmetry, also called full-slip, boundary condition is applied at the top, bottom and side boundaries.

As for the initialization of the domain, it was found that ANSYS' Hybrid initialization produced good results. In contrast to the standard initialization in Fluent, hybrid initialization solves the Laplace equation to obtain a velocity- and pressure field. The remaining variables, which in this case is the turbulence is patched based on average values through the domain.

4.2.3 Numerical Setup

By recommendations from ANSYS [2], the PISO algorithm with neighbour correction was used for the pressure-velocity coupling as the simulation is transient. This generally enables the use of larger time-steps during calculations and thus reduces the total amount of steps needed. For the spatial discretization, the gradients are calculated using the Least Square Cell Based scheme, whilst the pressure is calculated using the second Order scheme. To achieve high accuracy in the solution the Second Order Upwind scheme has been used for the equations of momentum, turbulent kinetic energy k and dissipation rate ε. An overview of the schemes used is given in Table 3.

Table 3: Simulation solver setup used in ANSYS Fluent.

Setting	Option
Pressure-Velocity Coupling	PISO
Gradient	Least Square Cell Based
Pressure	Second Order
Momentum	Second Order Upwind
Turbulent Kinetic Energy	Second Order Upwind
Specific Dissipation Rate	Second Order Upwind
Transient Formulation	Bounded Second Order Implicit

A study of the discretization schemes and pressure-velocity coupling was not performed as it has not been in the scope of this thesis. However, simulations using the SIMPLE pressure-velocity coupling were conducted to ensure reliable results.

It was found that the simulation was stable when under-relaxation factors were set to 1 (no under-relaxation), and it was therefore used for all equations in the simulations to speed up convergence and thus reduce the computational cost. In accordance with ANSYS recommendations it was found that approximately 10 iterations were necessary per time-step to achieve sufficient convergence [2].

As the transient formulation used in the simulations are of the implicit type, no stability criteria are determinant in the selection of the time-step Δt as for example the Courant-Friedrichs-Lewy condition. It was found that starting the simulations at a time-step of $\Delta t = 5 \cdot 10^{-6}$s and gradually increasing the time-step up to $\Delta t \approx 1.5 \cdot 10^{-5}$s over a few hundred iterations worked well when executing the simulations. Where the time-step of $\Delta t \approx 1.5 \cdot 10^{-5}$s functioned as a limit for obtaining necessary convergence in the simulations. To obtain a developed flow approximately 0.1s (7000 iterations) were necessary. It was attempted to reduce this development time by computing a steady state solution as an initial condition for the transient calculation. However little improvement in computational time was achieved.

4.3 System Coupling

Two FSI cases are conducted with a inlet flow velocity of 19m/s and 20m/s. As the mesh generation is based on the 20m/s case it is considered that the meshing will be appropriate for a case with a slightly lower inlet flow velocity. Hence, the only difference in the setup of the cases are the inlet boundary condition in Fluent. Each of the systems is set up in their respective solvers as described in Section 4.1 and 4.2, before being fed into the System Coupling application. Detailed reports regarding the setup of the individual systems are given in Appendix C and D. The full fluid-structure interaction system setup in Workbench can be seen in Figure 14.

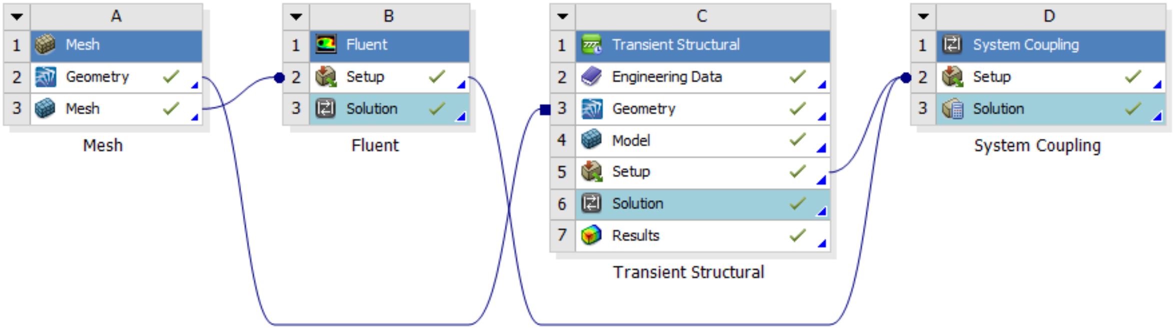

Figure 14: Workbench setup for Fluent and Mechanical system coupling.

Prior to starting any multi-physical simulation using system coupling, the coupling itself has to be set up. This setup is composed of three main areas.

Analysis Settings defining initialization, duration and step controls. The time-step specified here will work as a global governing step size in which the participating systems will follow. In this case, the Fluent model requires the smallest time-step and is therefore used for the FSI calculations. Furthermore, the minimum and maximum number of coupling iterations per time-step has to be set. In the simulations in this thesis the min/max coupling iterations is set to 1/2 as it only is a one-way coupling.

Data Transfers defining the source/target, transfer variable and data transfer control. Depending on the coupling type a variety of combinations can be specified. In this one-way coupling, the force from the Fluent cylinder face is defined as the source and the target in Mechanical is specified as the Fluid Solid Interface discussed in Section 4.1.2. The data transfer convergence criterion is set to 0.01 and no under-relaxation factor or ramping is used in the calculations.

Lastly, the *Execution Control* has to be specified. Here the simulation sequence, specifying the solver order is set to Fluent (1) and Mechanical (2). A variety of expert settings is also available under execution control, however, these are left unattended as they are not relevant to this current case.

5 Validation cases

As the final model is a result of building systematically increasingly complex models, each of these subsystems will be presented prior to the full FSI model in this section. The validation of the CFD model is presented with the cases of a 2D cylinder flow, 3D straight cylinder flow and lastly the tapered cylinder. As for the CSD model, a mesh refinement and modal analysis are presented.

5.1 CFD

Evaluation of the validity of the model has been based on the forces acting on the cylinder. Statistical quantities such as the magnitude of the drag- and lift component, as well as their corresponding frequencies, is sampled over a minimum of 20 periods in a fully developed flow to obtain a representative value. These statistics are then compared to similar data of supercritical flow around cylinders obtained from numerical- and experimental studies conducted in the past [7][11][28][34].

5.1.1 2D Case

The basis of the CFD model is a simple 2D model of flow over a circular cylinder. Due to the accessibility of relevant data and that the shedding frequencies of interest are apparent for Reynolds numbers in the range of $9 \cdot 10^5 < \mathrm{Re} < 1.1 \cdot 10^6$ the base case is simulated at a Reynolds number of 10^6. The results of the mesh refinement study of the 2D case are listed in Table 4.

Table 4: 2D mesh refinement study of the parameters in the refined region surrounding the circular cylinder. The refinement parameters used are the number of radial elements in the refinement region N_r and the number of peripheral elements on the cylinder N_θ.

	N	N_r	N_θ	St	$C_{D,mean}$	$C_{L,RMS}$
1	8871	30	100	0.3349	0.4565	0.1360
2	18604	35	200	0.3612	0.4481	0.1085
3	21597	40	200	0.3602	0.4446	0.1097
4	31432	50	300	0.3621	0.4434	0.1091

It can be observed that the vortex shedding frequency and force coefficients are slightly dependent on the peripheral element distribution N_θ. Furthermore, the Strouhal number is within the expected range for a smooth cylinder at this Reynolds number. It was concluded that a N_θ of 200 and N_r of 40 is sufficient to obtain a mesh independent solution and thereby used as the mesh parameters in the later cases.

5.1.2 3D Straight Cylinder Case

By using the peripheral and radial mesh parameters obtained from the 2D model, a mesh refinement study of a 3D straight cylinder with the same dimension as the 2D model was conducted. As it is concluded that the parameters N_θ and N_r are sufficient, the refinement technique in 3D is based on the distribution in the z-direction. The number of nodes in the $z-$direction is increased gradually and minor changes in the face sizing are made to preserve high quality elements for the given mesh. The results of the 3D mesh refinement are listed in Table 5.

Table 5: 3D mesh refinement study with increasingly more number of spanwise nodes of flow around a stationary straight cylinder.

	N	N_z	St	$C_{L,RMS}$	$C_{D,mean}$
1	304880	20	0.3539	0.0875	0.4352
2	685360	40	0.3546	0.0912	0.4368
3.	913080	60	0.3556	0.0927	0.4386
3	1118760	80	0.3507	0.0935	0.4332

As seen in Table 5 a reduction in both St, $C_{L,RMS}$ and C_D from the 2D case has occurred. Which can be related to the three-dimensional effects that are introduced in the model. Based on the observations from the mesh refinement, it was here concluded that a spanwise mesh distribution of $N_z = 80$ is sufficient to obtain necessary mesh independence, i.e. a cell height of 3.6 mm.

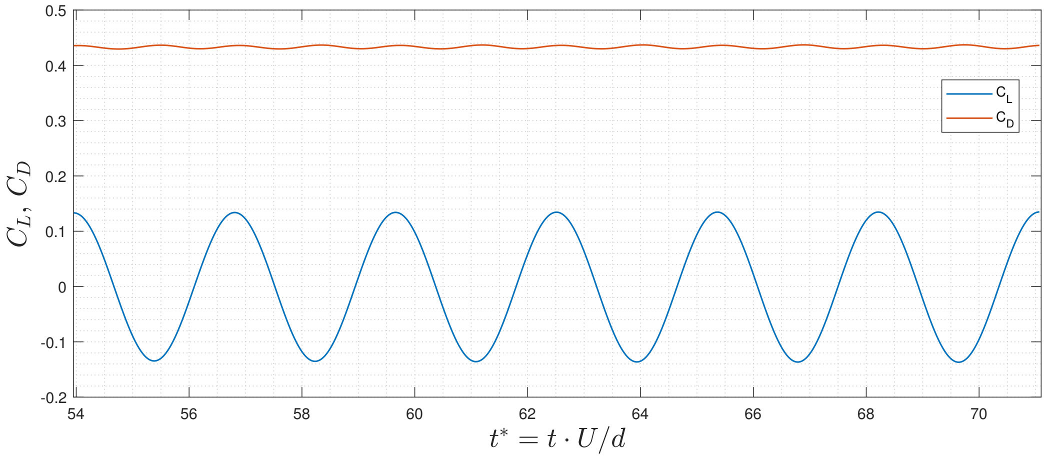

Figure 15: Section of the dimensionless time history of the force coefficients of the 3D straight cylinder case.

A sample of the lift and drag coefficient is shown in Figure 15. As seen, the lift oscillates with a mean value of 0 and an amplitude of approximately 0.13. The drag coefficient on the other hand has a mean value of 0.43 and a frequency twice as large as the lift. It can further be observed that the amplitude of the drag oscillations are significantly lower than that of the lift.

A comparison of the current 2D and 3D straight cylinder simulations and relevant data from the literature are given in Table 6. It shows that the results both based on the force coefficients and vortex shedding frequencies are well within their expected range. The calculated drag coefficient is slightly higher than LES-based models and experimental data. This is a commonly observed feature when utilizing RANS models and can be an effect of the fundamental differences between the models. The realizable $k - \varepsilon$ models all turbulent structures while LES only models the small scale turbulence. LES should in theory therefore more accurately model the turbulence in the cylinder wake which is a critical region to the calculation of the drag forces on the body. The lift coefficient on the other hand is captured well compared to the published data.

Table 6: A selection of results from similar studies of flow around a circular cylinder at Re = 10^6.

	$C_{D,mean}$	$C_{L,RMS}$	St
Present 2D	0.4434	0.1091	0.3629
Present 3D	0.4332	0.0935	0.3507
Catalano et al. [7] 3D LES	0.31	-	0.35
Catalano et al. [7] URANS	0.41	-	-
M.C. Ong et al. [28]	0.5174	0.0901	0.2823
Delany & Sorensen* [11]	0.286-0.405	-	0.379
Schmidt* [34] exp.	-	0.070	-

*experimental studies

5.1.3 3D Tapered Cylinder Case

From the conducted 2D and 3D mesh refinement study the parameters for N_θ, N_r and N_z is determined. An additional refinement of the spanwise mesh distribution N_z was conducted to verify that the parameters were valid with the introduced taper of $l/(d_0 - d_1) = 58$ and negligible effects were observed.

A section of both the lift and drag coefficient is shown in Figure 16. The effect of the taper becomes clear compared to Figure 15 where both the frequency and amplitude of the lift are no longer near constant. This is an effect of the non-constant diameter over the span of the cylinder causing a difference in the shedding frequency over the cylinder. The varying amplitude of the lift and drag is an effect of the constructive and destructive interference between these different shedding frequencies. This is also apparent in Figure 16b where a second much longer interference-period is seen from $t^* = 75$ to t^*125.
This can be further demonstrated by the frequency spectrum of the lift coefficient shown in Figure 18. The dominating shedding frequencies are centered around 250 Hz, however a second less powerful frequency around 270 Hz is apparent due to lower diameter at the top of the cylinder.

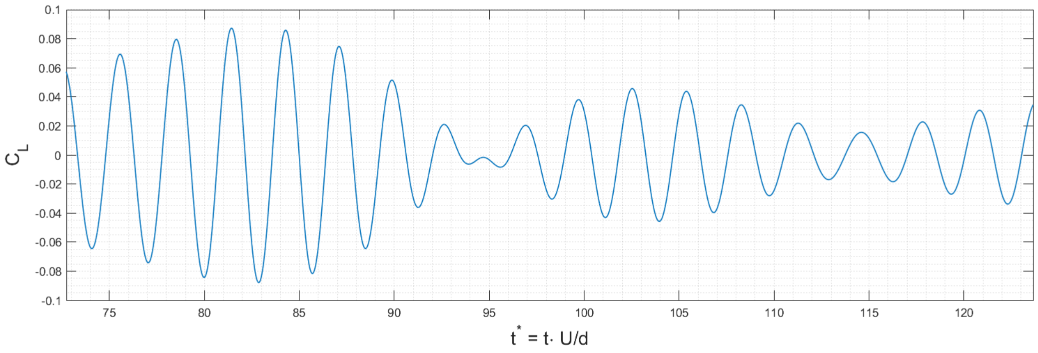

(a) Lift coefficient.

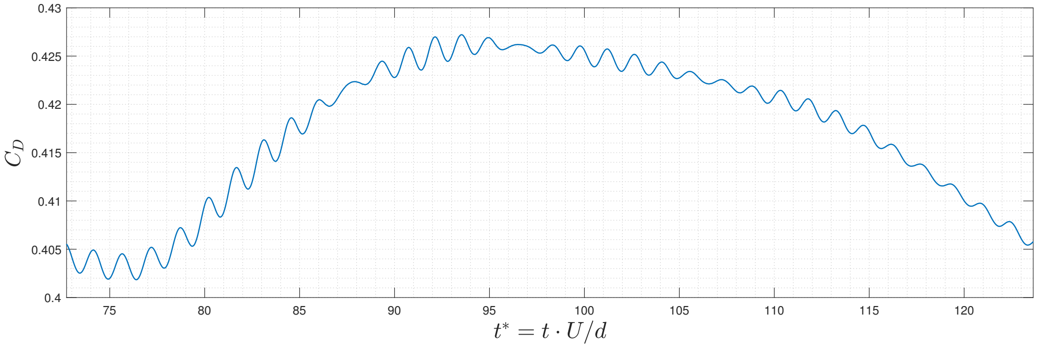

(b) Drag coefficient.

Figure 16: Section of the dimensionless time history of the lift (a) and drag (b) coefficients of the 3D tapered cylinder case.

Figure 17 shows a section of the y-component of the velocity behind the cylinder. It clearly shows one of the effects of the tapering of the cylinder. The bending of the vorticity structures in the wake towards a horizontal positions are similarly observed in the studies conducted on flow around tapered cylinders [30][26].

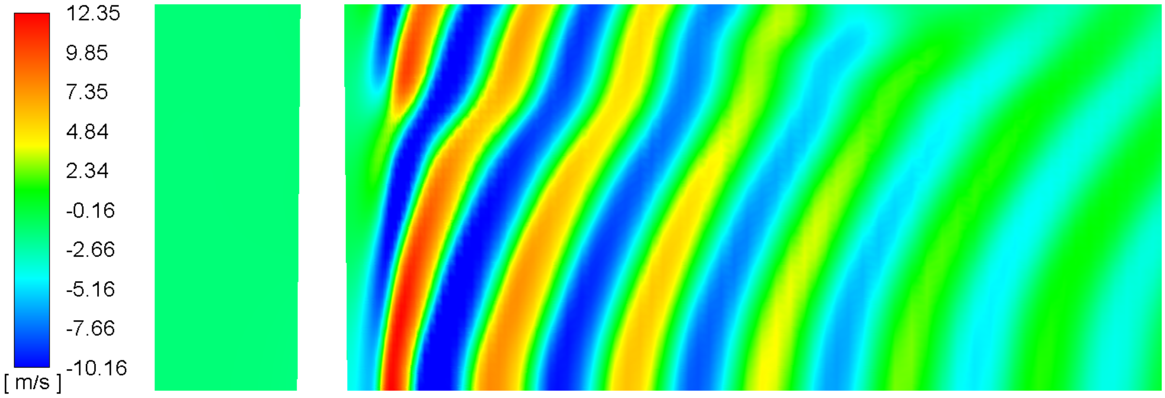

Figure 17: Close up contour plot of the y-velocity. Plane located in the x-z direction with a center in y = 0.

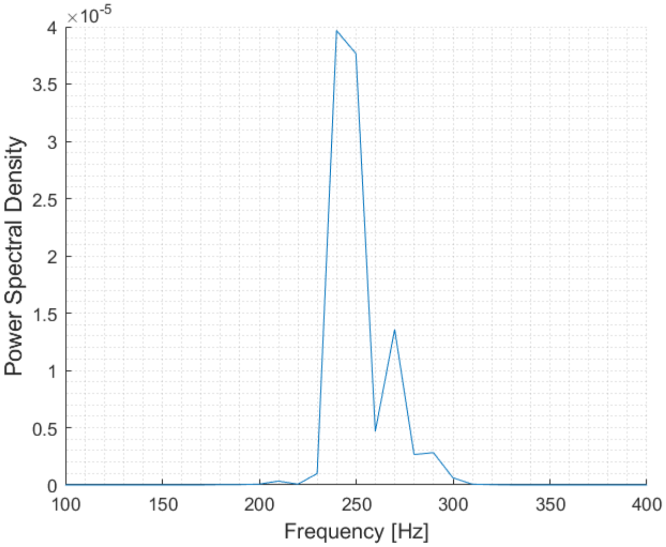

Figure 18: Fast Fourier transform showing the power spectral density of the lift coefficient for the tapered cylinder case.

5.2 CSD

The validation of the structural model in ANSYS Mechanical is based on conducting a mesh refinement study and a modal analysis. The mesh refinement is conducted as a transient case with an applied step load and assessed on the basis of the maximum deflection and von Mises stress. The modal analysis assessed based on calculations done by DNV-GL and a simplified analytical case.

5.2.1 Mesh Refinement

It was observed that the displacement of the structure was not affected to a noticeable extent by the mesh refinement. However, both the stress concentration and its location was found to be highly dependent on the refinement. With an increasing number of elements it was observed that the stress concentration moved from the cylinder towards the filleted transition between the cylinder and flange. A total of 6 refinements were completed and the results of the mesh refinement on the normalized maximum von Mises stress σ_e and normalized tip deflection is shown in Figure 19.

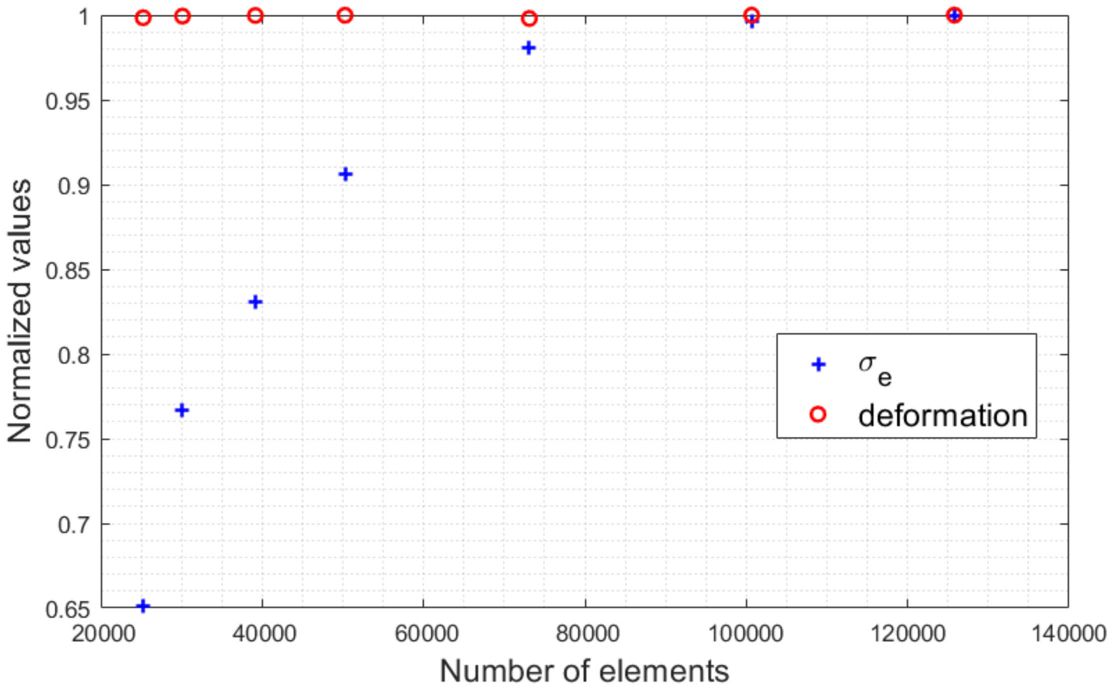

Figure 19: Mesh refinement study of the thermowell. Normalized values of the deformation and maximum von Mises stress σ_e.

As indicated in Figure 19 it was found that around 100.000 elements were sufficient to produce a converged stress concentration at the sharp re-entrant corner between the cylinder and flange. Between the two simulations with the highest resolution a relative change in

$\sigma_e < 1\%$ was observed and no change in the maximum tip-deflection. Thus the model is considered to be mesh independent at the last two simulations conducted with 100665 and 125789 elements.

5.2.2 Modal Analysis

The modal analysis was conducted in order to ascertain the natural frequencies of the system. The thermowell and small-bore connection system are fixed at the end of the small-bore connection, and the independent mesh from the refinement study is used. In order to ensure that all relevant and critical natural frequencies are captured the first 6 modes are calculated. The results from the modal analysis are listed in Table 7.

Table 7: The 6 first mode shapes with associated natural frequencies f_n for the thermowell/small-bore component.

Mode shape	Natural frequency f_n
1	238.43 Hz
2	238.44 Hz
3	524.78 Hz
4	527.21 Hz
5	527.24 Hz
6	1288.4 Hz

Where the 1st and 2nd mode represents cantilevered bending shapes of the thermowell cylinder in in-line and crossflow direction. The 3rd represents a compression shape which is of no interest in this case due to the absence of compressive forces in the flow. The 4th and 5th mode shape show bending shapes of the flange. While lastly, the high-frequency 6th mode represents the typical S-shape bending. The modal shapes for the natural frequencies of 238.4 Hz and 527.2 Hz are shown in Figure 20a and 20b respectively.

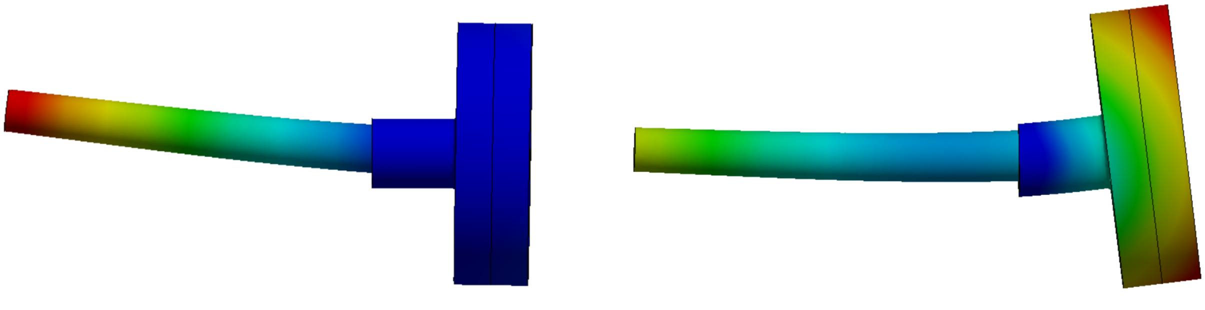

(a) 1st mode shape for the corresponding natural frequency $f_n = 238.43$ Hz.

(b) 4th mode shape for the corresponding natural frequency $f_n = 527.21$ Hz.

Figure 20: First and fourth mode shape of the thermowell. It should be noted that the deformation is not in true scale.

From the modal shapes and frequencies, it is evident that the 1^{st} and 2^{nd} mode with natural frequencies of 238.4 Hz is the critical ones. This because of operating conditions that will not result in shedding frequencies as high as 527.21 Hz. The 1^{st} and 2^{nd} natural frequencies are in good compliance with DNV-GL's prior simulations and measurements. A first natural frequency of 238.43 Hz is also in good compliance with the simplified case of a cantilevered beam calculated to a natural frequency of 230Hz. For details regarding the analytical solution see Appendix A.

6 Results and discussion

In this section, the results from the FSI calculations are presented. From the validation cases discussed in Section 5.1 and 5.2 the participating fluid and structural systems are coupled together to a FSI-model. The results from the FSI calculations are given in the form of structural response and fluid forces. Two FSI cases with an inlet flow velocity of 19m/s and 20m/s were conducted to ensure that the resonant effects were captured. To show the difference in the structural response of the two cases, they are presented and discussed in parallel.

6.1 Fluid-Structure Interaction

The total tip deflection of the thermowell can be seen in Figure 21 and Figure 22. As the fluid-structure density ratio is as low as $\rho_f/\rho_s = 0.01$ and that the thermowell is constructed of steel, the deflections are in the order of only 0.1 mm in both cases. This is a good indication that the one-way fluid-structure interaction model is appropriate to use in this case. As the deformations are very small the fluid-structure boundary will not be strongly altered by the deforming thermowell. If this was not the case, the flow would be affected to a noteworthy extent as the boundary conditions are constantly changing. Hence a two-way fluid-structure interaction model accounting for the deforming body should then be implemented.

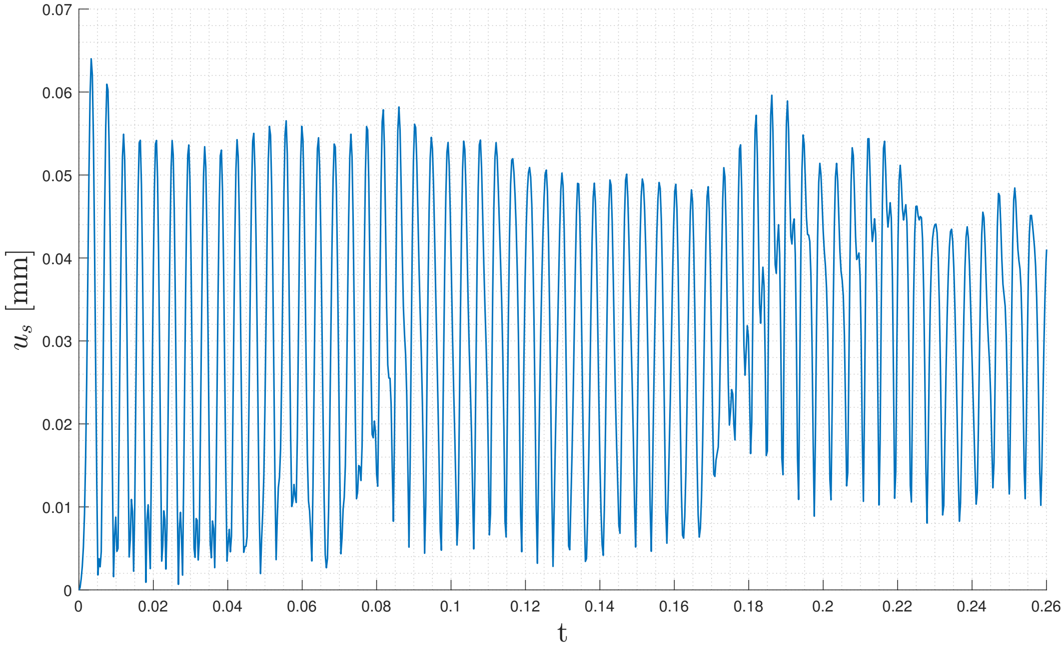

Figure 21: Time history of the maximum tip-displacement of the thermowell. Fluid-structure interaction case with flow velocity of 19m/s.

Even though both cases operates with deformations of a similar order of magnitude, the development differs with time. As seen in Figure 22, the tip deflection seems to reduce constantly, while in Figure 21 this is not the case. The fact that the case of 19m/s yields slightly lower forces due to vortex shedding, yet still results in higher deformations than the case of 20m/s indicates that cross-flow resonance is occurring in this case. The magnitudes of the lift- and drag forces for both cases can be seen in Figure 39 and Figure 40 in Appendix B.

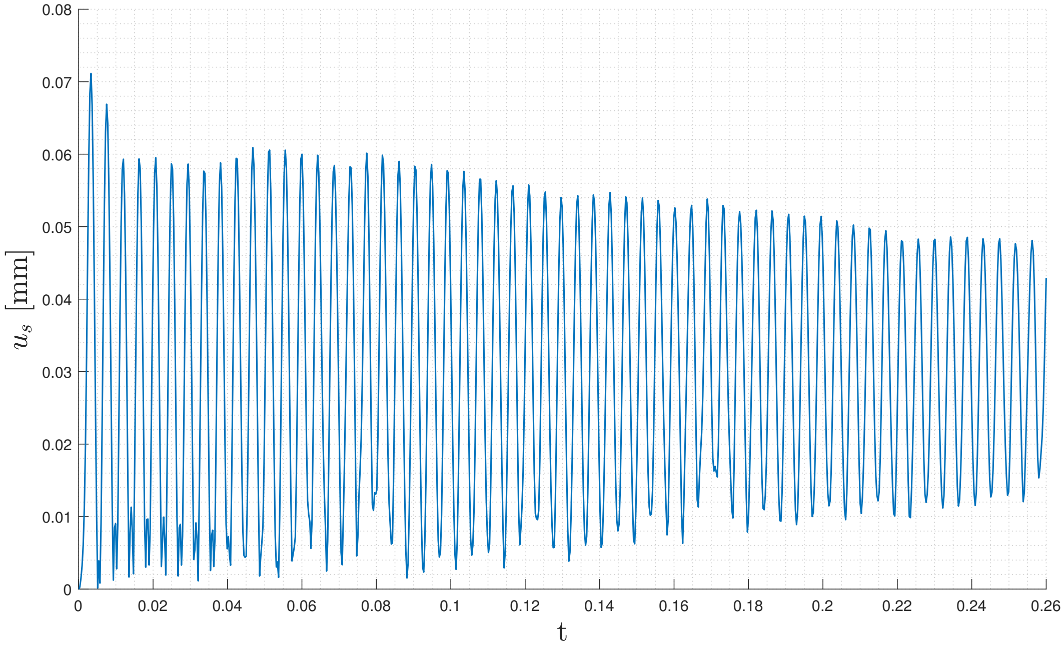

Figure 22: Time history of the maximum tip-displacement of the thermowell. Fluid-structure interaction case with flow velocity of 20m/s.

The in-line tip displacements for both cases are shown in Figure 23 and Figure 24. In contrast to the total tip displacement, the two cases behave quite similarly with only small differences in magnitude. As seen here, compared to the total tip-deflection in Figure 21 and Figure 22, the in-line deformations account for the majority of the total tip displacement at the beginning of the simulation. Further, the deflection in the in-line direction is monotonically decreasing over the time-interval 0-0.26s. Thus, no resonance is occurring in the in-line direction which is consistent with findings from DNV [12] and of course to be expected due to the oscillating frequency of the drag force. From the resting position at t=0, the thermowell experiences significantly larger deflections during the start-up of the system. This can be explained by the development of the drag-coefficient where the forces in the in-line directions are larger than that of the developed flow which can be seen in Figure 31 and Figure 32.

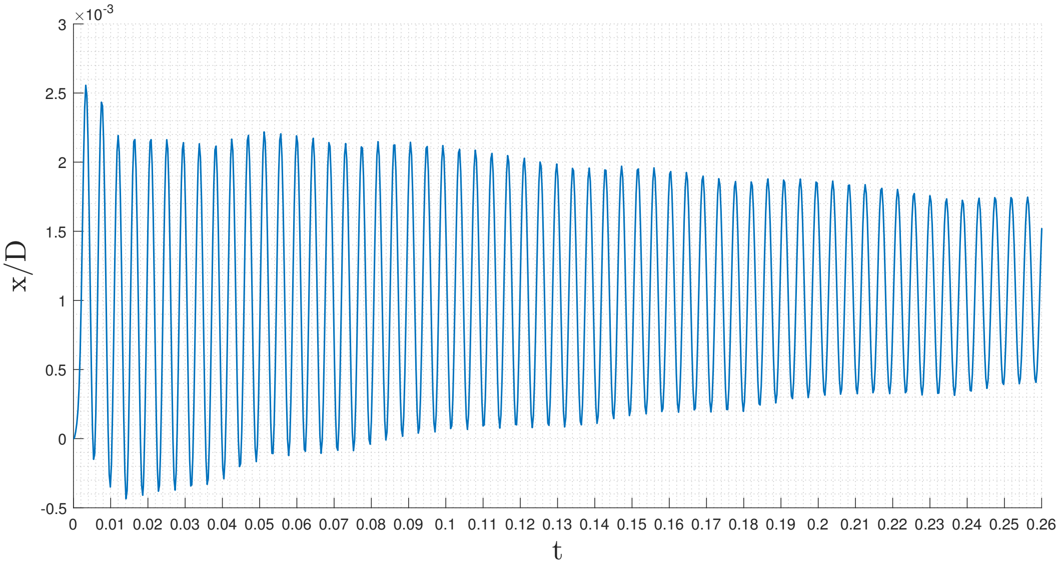

Figure 23: Development of the in-line thermowell tip displacement. Fluid-structure interaction case with flow velocity of 19m/s.

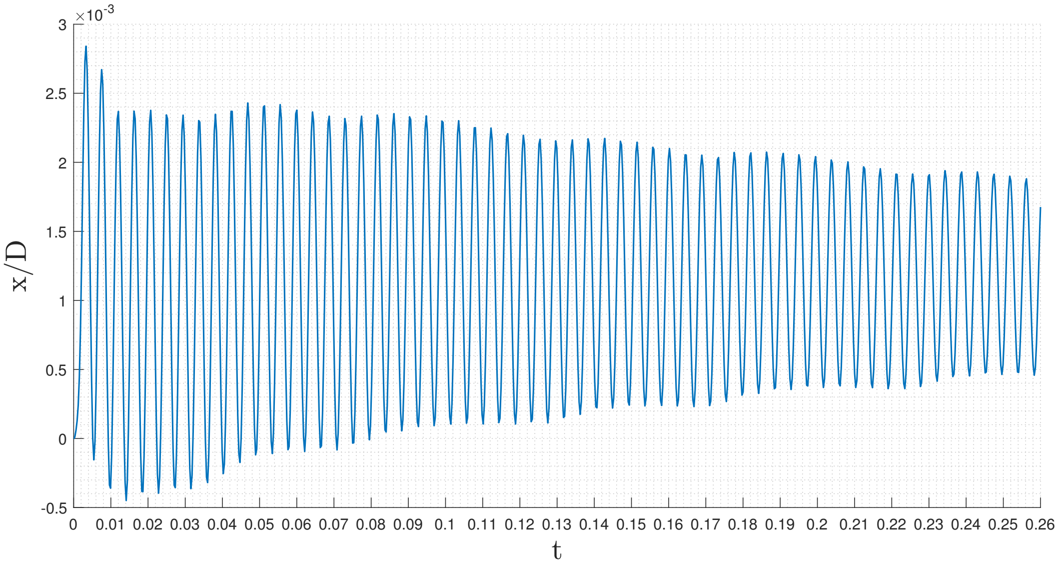

Figure 24: Development of the in-line thermowell tip displacement. Fluid-structure interaction case with flow velocity of 20m/s.

The cross-flow tip displacement is shown in Figure 25 and Figure 26. As the cross-flow tip displacement is a result of the lift force from the fluid, the deformations are relatively small in the beginning as the vortex shedding is under development. In contrast to the in-line displacements, the cases differ significantly with regards to the cross-flow displacements. In the case of 19m/s cross-flow amplitudes of $y/D \approx 1.7 \cdot 10^{-3}$ is occurring as opposed to the case of 20m/s where a maximum amplitude of $y/D \approx 7 \cdot 10^{-4}$ is observed. This, even though that the cross-flow forces are lower in the 19m/s case. By performing a static analysis with a force of 5N, similar to the maximum magnitude of the cross-flow force, a maximum tip deflection of $y/D = 1.467 \cdot 10^{-4}$ is obtained. Compared to the maximum deflections from the transient FSI calculations it can be observed that the deflections in the case of 19m/s are amplified by a factor of 12, while the case of 20m/s, by a factor of 5.

In the case of 19m/s both the maximum cross-flow and in-line deflection is in a similar order of magnitude, whereas in the case of 20m/s the maximum deflection is approximately 3 times smaller in the cross-flow direction than the in-line direction. However, the forces acting on the thermowell is approximately 6-7 times larger at its peaks in the in-line direction. On average, the in-line forces are even larger compared to the cross-flow due to the varying amplitudes of the lift. These relatively high deflections compared to the forces acting in the cross-flow directions can be explained by the fact that the forces oscillate around 0 and near the natural frequency of the structure. In fact, a frequency ratio of $f_v/f_n \approx 1.04$ is obtained for the case of 19m/s, whereas a ratio of $f_v/f_n \approx 1.09$ is observed in this case of 20m/s. Which indicates that the structure in both cases should be in the region exposed to the cross-flow resonance discussed in Section 3.3.6.

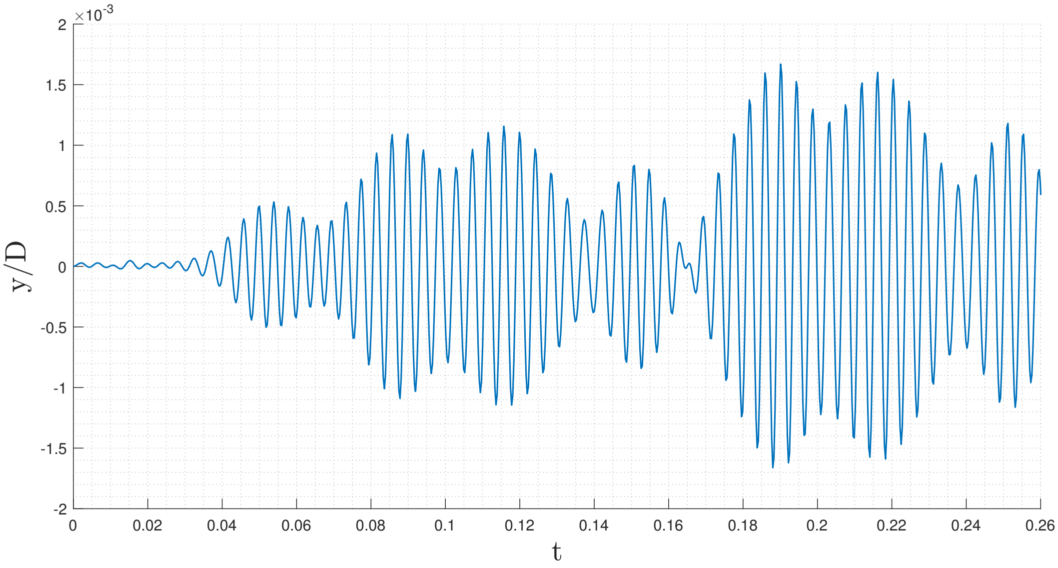

Figure 25: Development of the cross-flow tip displacement. Fluid-structure interaction case with flow velocity of 19m/s.

By combining the in-line and cross-flow displacements, the time history of the tip position is obtained. Unlike observations done on FSI simulations of vortex-induced vibrations for risers etc. where structured patterns can be observed [15][23][37], the tip-displacement does not show a clear pattern of movement. The history of the tip-position for both cases can be seen in Figure 36 and Figure 37 in Appendix B. As seen here, both cases have a relatively ordered pattern in the x-direction where a nearly constant frequency and a reduction in the amplitude is observed. However, the movement in the y-direction does not seem to follow any trends. There are obviously significant differences between this thesis and the studies, which can help explain why no pattern is observed. The density ratio is significantly lower in this study, which results in a weaker interaction. In this study, the thermowell is only fixed at one end as opposed to both ends. And lastly, the observations are seen on cylinders with a uniform cross-section which yields a more evenly distributed force as opposed to the tapered thermowell.

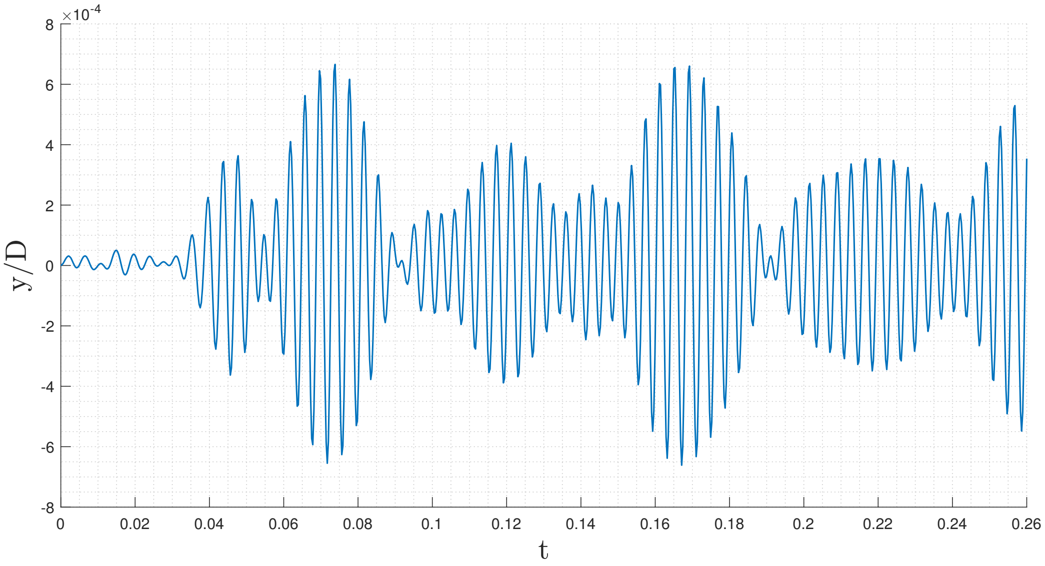

Figure 26: Development of the cross-flow tip displacement. Fluid-structure interaction case with flow velocity of 20m/s.

The velocities at the tip of the thermowell and at the tip of the flange for the cases of 19m/s and 20m/s is shown in Figure 27 and Figure 28. As expected the thermowell tip velocity is significantly higher than the flange velocity in both cases. This due to the fact that the fluid force acts on the cylinder and the location of the constraint at the small-bore connection, thereby acting almost as a cantilevered beam with a distributed load.

A clear difference in the response of the structures can be observed between the two cases. In the case of 20m/s, both the tip and flange maximum velocities are decreasing towards a response with a maximum velocity of approximately 30mm/s. Again, this indicates that the structure is not in cross-flow resonance, where the velocities should be expected to be amplified due to increasing deformation-amplitudes. In contrast, the development in the case of 19m/s shows a significantly different response. In the region $0 < t < 0.08s$, where the lift-force is not yet fully developed, the response is quite similar with regards to the amplitudes, which is expected as drag is the dominant force here. However, beyond $t = 0.08s$ the fluctuations become smaller until approximately $t = 0.16s$. This is a result of a more circular motion, as can be seen in Figure 36 in Appendix B, where the structural motion is not turned as abruptly. Thereby, smaller fluctuations occur. Beyond $t = 0.16s$ a significant increase in the tip-velocity occurs, with amplitudes up to 65mm/s. This indicates that the thermowell is experiencing resonance, which can be further backed up by observing the tip-position in Figure 36. Here, the last interval corresponds to the cross-flow dominant motion associated with a resonant response.

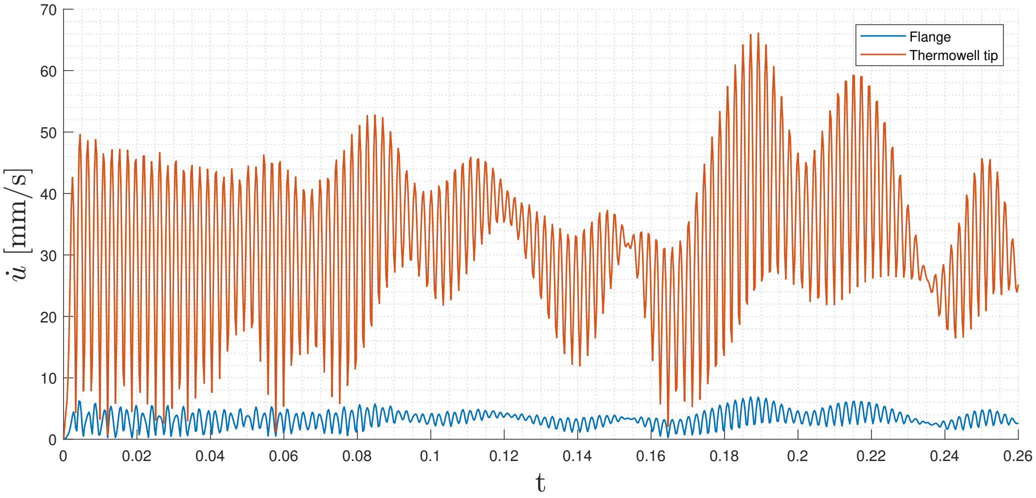

Figure 27: Development of the velocities at the thermowell tip and flange. Fluid-structure interaction case with flow velocity of 19m/s.

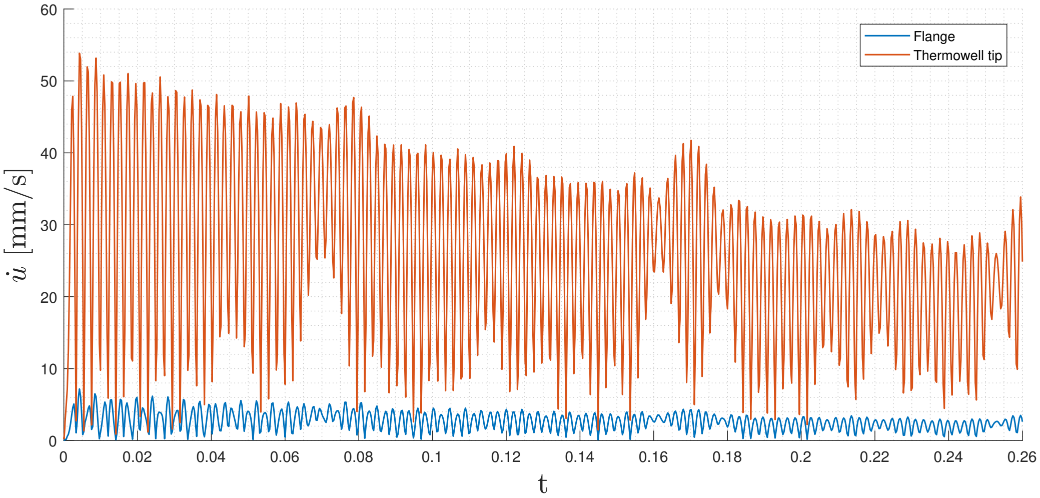

Figure 28: Development of the velocities at the thermowell tip and flange. Fluid-structure interaction case with flow velocity of 20m/s.

In the evaluation regarding the severity of the thermowell vibrations, the vibrational velocities are often used as a measure. According to industry standards (Ø. Bye DNV-GL 2019, personal communication, 20. February), vibration levels inside the thermowell should fall below 10 mm/s RMS. If vibration levels are in between 10 mm/s and 31 mm/s further investigation is advised. While vibration levels above 31 mm/s RMS require preventive measures to be implemented.

The vibrations in the case of 20m/s are calculated to be 28.79 mm/s RMS if the full sample is used and 22.08mm/s if sampled in the more developed region $0.2 < t0.26s$. Whereas for the case of 19m/s a value of 34.15mm/s RMS is obtained by sampling the whole interval and even higher if the values are obtained when sampling later intervals. By applying these criteria to the two FSI cases it can be concluded that the integrity of the thermowell in resonance is exposed. As for the case in Figure 28 the vibrational levels do not exceed the critical limit, yet it does not fall under the acceptable limit either. Thus the vibrational levels cannot be used to evaluate the integrity of the structure on its own.

The ratio between the velocities at the tip of the thermowell and at the tip of the flange for the cases of 19m/s and 20m/s is shown in Figure 29 and Figure 30. A clear trend of a ratio $\dot{u}_{flange}/\dot{u}_{thermowell} \approx 0.10$ can be observed throughout the majority of the sampled time in both cases. During the development, some deviations from this trend can be observed where the flange and tip velocities are out of phase. The deviations are slightly more prominent in the case of 20m/s. However, this effect is suppressed with time and nearly invisible for $t > 0.1$s in both cases. The fact that the thermowell tip and flange velocity show a nearly constant ratio could be explained by the fact that the forces acting on the thermowell are small. Thus, the response of the structure is defined by linear deformation.

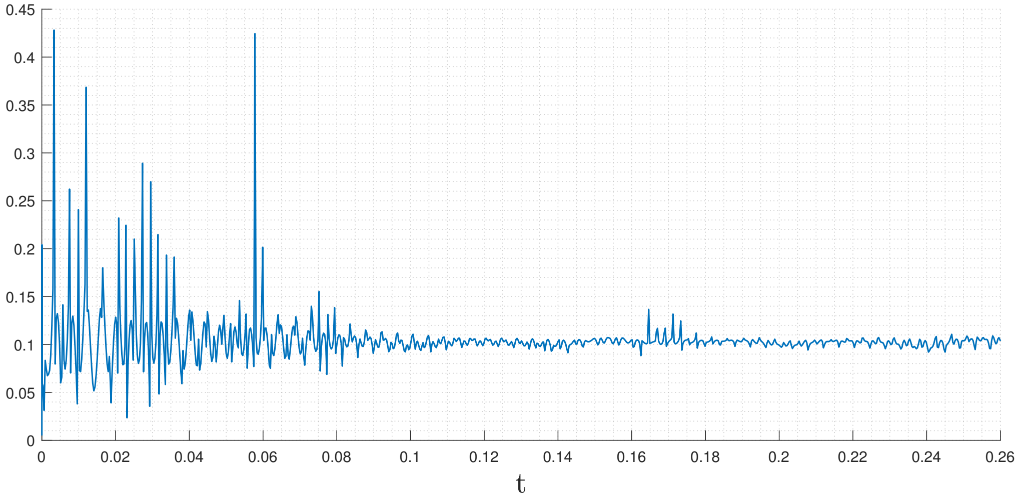

Figure 29: Ratio of the thermowell tip and flange velocities. Fluid-structure interaction case with flow velocity of 19m/s.

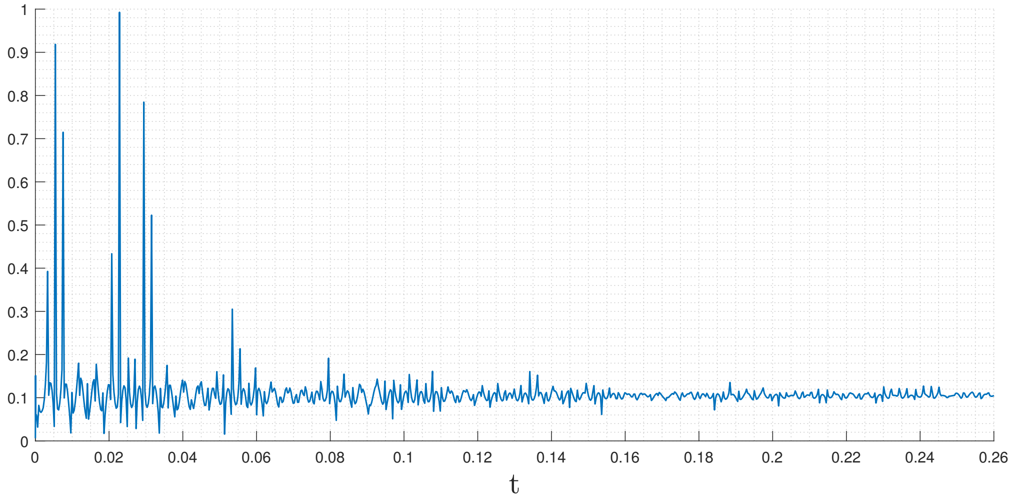

Figure 30: Ratio of the thermowell tip and flange velocities. Fluid-structure interaction case with flow velocity of 20m/s.

The development of the force coefficients in the cases of 19m/s and 20m/s is shown in Figure 31 and Figure 32. As seen, the force-coefficients from the fluid behaves quite similar with regards to the magnitudes, which is to be expected for Reynolds numbers in this region. However, a small change in the vortex shedding frequency occurs between the 19m/s and 20m/s cases.

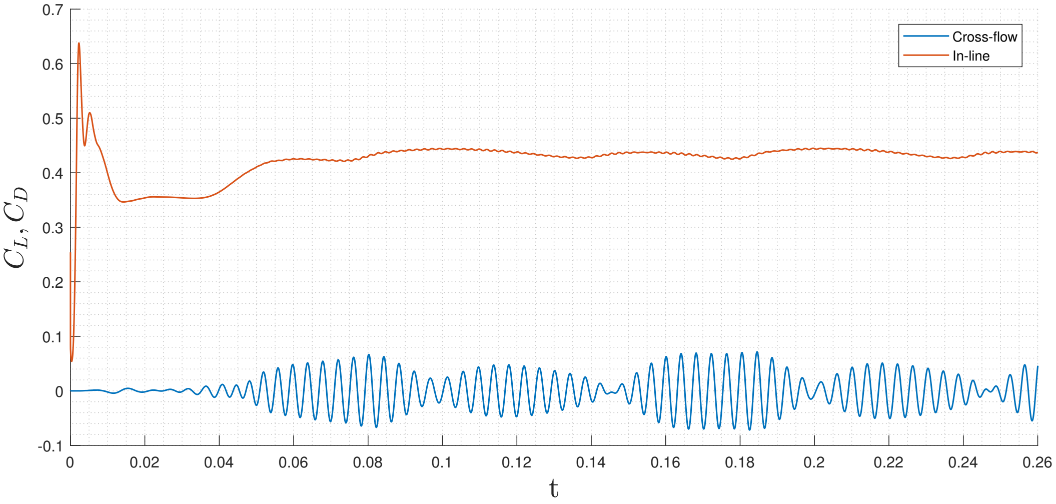

Figure 31: Development of the force coefficients. Fluid-structure interaction case with flow velocity of 19m/s.

The effects of the tapered cylinder can clearly be seen in both the drag- and lift coefficient. Due to the non-uniform cylinder diameter both the lift- and drag coefficient varies in magnitude with time. Similar development of the force coefficient is observed for flow around tapered cylinders in the literature [33]. This is an effect of the interference of the varying shedding frequencies along the span of the thermowell. At the root of the well where the diameter is 28.76mm, the flow has a Reynolds number of $1.046 \cdot 10^6$, whereas at the tip of the well with a diameter of 25mm has a Reynolds number of $0.909 \cdot 10^6$. As discussed in Section 3.1 and 3.2.5 this should cause both a lower drag- and lift coefficient for the sections with Reynolds numbers approaching $9 \cdot 10^5$. This due to the fact that it approaches the drag crisis region of $Re_c \approx 5 \cdot 10^5$.

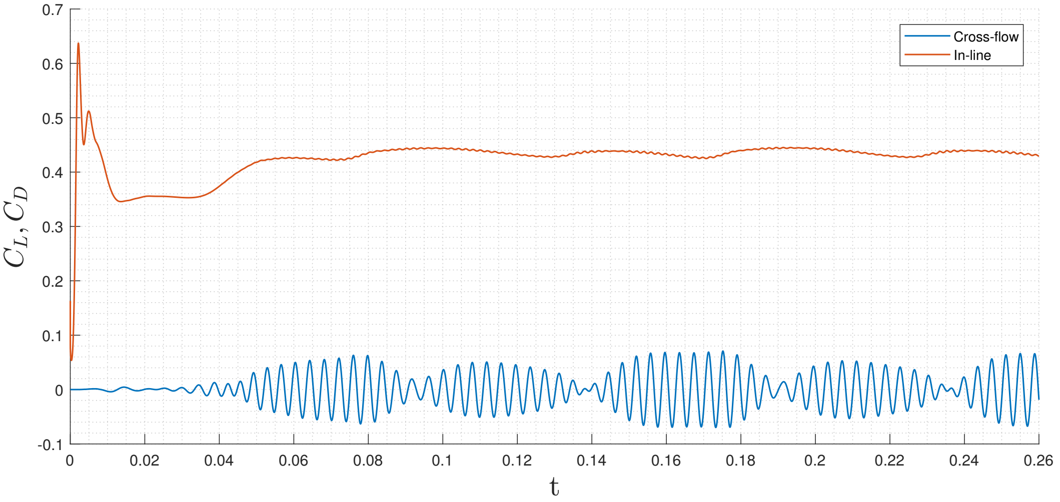

Figure 32: Development of the force coefficients. Fluid-structure interaction case with flow velocity of 20m/s.

A Fast Fourier Transform of the lift coefficient for both cases is given in Figure 38 in Appendix B. As seen here, the dominant shedding frequency is different in the two cases. For the case of 19m/s, the dominant shedding frequency has a value of $f_v = 237\text{Hz}$ and $f_v = 250\text{Hz}$ for the case of 20m/s. Compared to the structure's natural frequency of $f_n = 238.43\text{Hz}$ given in Section 5.2, it becomes obvious that both cases are in the region where resonance can occur. However, the fact that the case of 19m/s shows stronger signs of resonance corresponds well with the given dominant shedding frequency, which is almost equal to the natural frequency of the structure.

The development of the maximum von Mises stresses in the thermowell and small-bore for the cases of 19m/s and 20m/s is shown in Figure 33 and Figure 34. By inspecting the development, a clear similarity to the total tip-deflection in Figure 21 and Figure 22 can be observed. This is, of course, to be expected due to the relationship between deformation and stress. As expected, due to the decreasing tip deflection seen in Figure 24, the maximum stresses are also decreasing throughout the interval. An example of the stress-distribution in the thermowell and the small-bore connection is shown in Figure 35. As expected the maximum stresses occur in the corner between the cylinder and flange in both components.

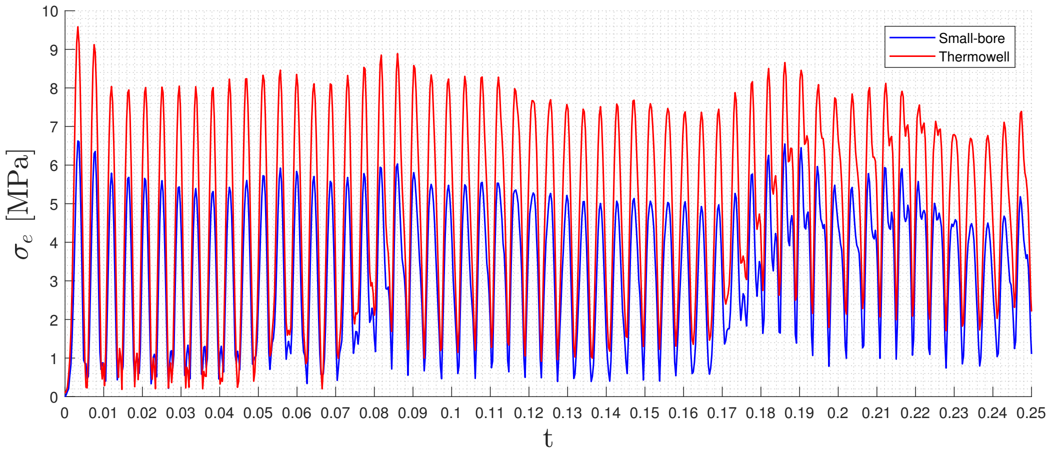

Figure 33: Development of the maximum von Mises stresses σ_e in the thermowell and small-bore connection. Fluid-structure interaction case with flow velocity of 19m/s.

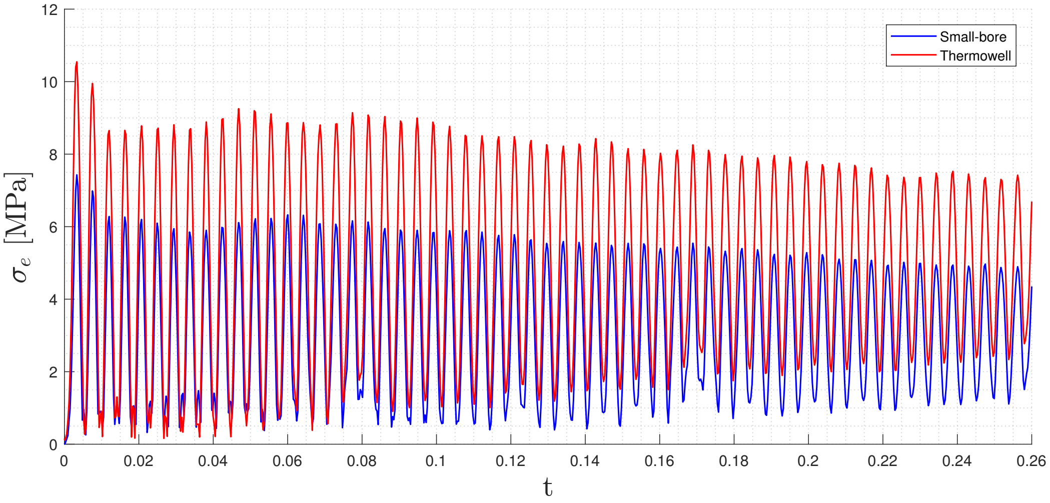

Figure 34: Development of the maximum von Mises stresses σ_e in the thermowell and small-bore connection. Fluid-structure interaction case with flow velocity of 20m/s.

To evaluate whether the stress concentrations are within an acceptable range, the criteria *Guidelines for the avoidance of vibration induced fatigue in process pipework* is applied to the components [13]. Here, a vibration criteria corresponding to a maximum stress level of 17.5 MPa (peak to peak) is stated as the acceptable limit.

As seen in Figure 33, the maximum stresses in the thermowell and small-bore connection differs with a magnitude in the range 2-3MPa. A difference between the thermowell and small-bore is of course to be expected by reviewing the geometries of the components. In contrast to the thermowell, the small-bore connection has a larger area to distribute the stresses over and thus experiences lower stress concentrations. Similar behaviour is observed for the case of 20m/s seen in Figure 34.

As seen in Figure 34 the stress levels in the structure exceed the criteria slightly during start-up of the system. However, for a developed flow the stress levels are well within the range of the criteria and should therefore not be at risk of fatigue due to the vibrations. Combining this with the criterion related to the vibrational velocities discussed earlier it can be concluded that vibrational velocities in the order of 22.08mm/s RMS does not pose a threat to the structure's integrity. In contrast, the thermowell in Figure 33 exceeds the maximum stress criterion in a few instances and can therefore be exposed to fatigue. This is in compliance with the criterion regarding the vibrational velocities where a RMS value above 31mm/s is said to be damaging to the structure.

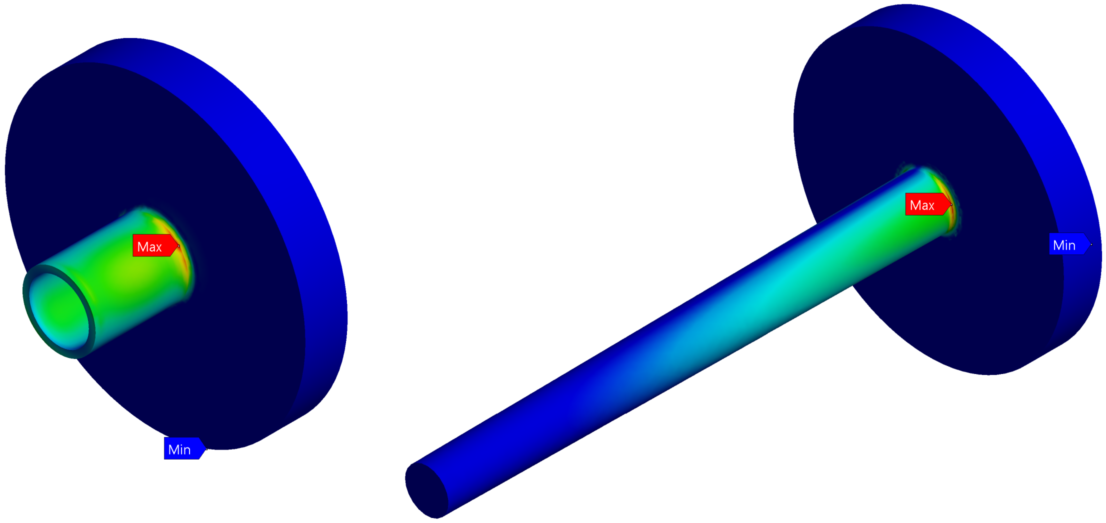

Figure 35: Example of the location of the maximum stresses in the thermowell and small-bore connection.

7 Concluding Remarks

This thesis presents a relatively simple fluid-structure interaction approach to the topic of flow-induced vibration using ANSYS Workbench. The fluid system is modelled using the Fluent solver, while the structural system is modelled using the Mechanical solver, both part of the multi-physics software of ANSYS. The fluid-structure coupling is conducted with the component System Coupling.

Two FSI cases were simulated with an inlet flow velocity of 19m/s and 20m/s with a corresponding mean Reynolds number of $\bar{Re} \approx 929000$ and $\bar{Re} \approx 977000$ to study the structural response of a thermowell in resonance. In the case with a flow velocity of 19m/s, a resonant response was obtained and evaluations regarding the integrity of the components are given. By reviewing the results, it is thereby concluded that:

- The one-way fluid-structure interaction simulations were able to capture cross-flow resonance of the thermowell.
- The results of the fluid-structure interaction simulations suggest that for low fluid/structure density ratios ($\rho_f/\rho_s < 0.01$), the thermowell will be exposed to damaging vibrations in resonant frequencies. While flow conditions in the vicinity of the resonant conditions the structure, even if not in resonance, approach the tolerated stress limit given by DNV [12].
- The resonance suppressing effect of the tapering can clearly be seen in the response of the system. And the amplification of the structural deflection seems to be limited by the varying cross-flow force amplitude and frequency from the vortex shedding.
- The results show that the flange and tip velocity follows a nearly constant ratio of 0.10. This could indicate that a general relationship can be expressed to be able to predict possible damaging vibrations based on measurements conducted at the flange. However, this needs further research.
- The results indicate that for low fluid/structure density ratios the use of a one-way fluid-structure interaction may be sufficient as opposed to the computationally expensive two-way interaction model. The FSI cases conducted in this thesis were completed with a CPU time in the range of 6-8 days for each case. Although this can be viewed as considerable CPU time, it is significantly less than the 6-8 weeks reported by Litteaur et al. [25].

7.1 Further Work

Although the model is able to produce good results, a few remarks can be made with regards to further validate or improving the model.

Due to the small forces, low fluid/structure density ratio and limited computational time the model used has assumed that a one-way coupling is valid in this case. However, even though the results indicate that a one-way model is sufficient, viscous damping and displacement of the structure could be of a non-negligible magnitude and should therefore be validated by comparing the results from a two-way FSI model to the results in this thesis.

With regards to the geometry of the case, the effect of the assumption that the pipe flow is of negligible importance should be incorporated into a new model, taking this into account to assess the validity of the statement. Furthermore, the model assumes that the cylinder is perfectly smooth, however in real life machined metal parts will have a certain extent of wall roughness. In the supercritical region, the Strouhal number varies significantly between smooth and rough surfaces and could therefore be further investigated. This however, requires more detailed data of the thermowell which was not available for this thesis.

Lastly, this thesis has been conducted using turbulence models based on the eddy-viscosity hypothesis. One of the assumptions behind the Realizable $k - \varepsilon$ is that the turbulence is isotropic, i.e $u_1 = u_2 = u_3$. To investigate if this assumption is valid an algebraic stress model or Reynolds stress model could be tested as these models are not based on isotropic turbulence.

References

[1] ANSYS, 2019. *ANSYS FLUENT Theory Guide (19.0 ed.)*, ANSYS INC.

[2] ANSYS, 2019. *ANSYS FLUENT User's Guide (19.0 ed.)*, ANSYS INC.

[3] ANSYS, 2019. *ANSYS Mechanical User's Guide (19.0 ed.*, ANSYS INC.

[4] ANSYS, 2019. *System Coupling User's Guide (19.0 ed.)*, ANSYS INC.

[5] Blevins, R.D., 1977. *Flow Induced Vibration*. Van Nostrand Reinhold Company New York.

[6] Blevins, R.D., Tilden, B.W., Martens, D.H., 1998. *Vortex-Induced Vibrations and Damping of Thermowells*, Journal of Fluids and Structures 12, 427-444

[7] Catalano, P., Wang, M., Iaccarino, G., Moin, P., 2003. *Numerical Simulation of the flow around a circular cylinder at high Reynolds numbers*, Int J Heat Fluid Flow 24, 463-9

[8] Cheah, J., (13.05.2017), *FEA Stress Singularities*,
https://www.ansystips.com/2017/05/fea-stress-singularities.html

[9] Chimakurthi, S.K., Reuss, S., Tooley, M., Scampoli, S., 2018. *ANSYS Workbench System Coupling: a state-of-the-art computational framework for analyzing multiphysics problems*, Engineering with Computers, 34:385-411

[10] De Nayer, G., Breuer, M., 2014. *Numerical FSI investigation based on LES: Flow past a cylinder with a flexible splitter plate involving large deformations (FSI-PfS-2a)*, International Journal of Heat and Fluid Flow 50, 300-315

[11] Delany, N.K., Sorensen, N.E., 1953. *Low-Speed Drag of Cylinders of Various Shapes*, NACA TN 3038.

[12] Det Norske Veritas, 2008. *Structural Analysis of Piping Systems*, Recommended Practice DNV-RP-D101.

[13] Energy Institute, (2nd Ed.) 2008 *Guidelines for the avoidance of vibration induced fatigue failure in process pipework*

[14] Guerrero, J., *Tips and tricks in OpenFOAM*, Module 9 - Lecture 1, Wolf Dynamics, http://www.wolfdynamics.com/wiki/OFtipsandtricks.pdf

[15] Han, X., Lin, W., Tang, Y., Zhao, C., Sammut, K., 2015. *Effects of natural frequency ratio on vortex-induced vibration on a cylindrical structure*, Computers & Fluids 110, 62-76

[16] Hansen, S.O., 2007. *Vortex-induced vibrations of structures*, Structural Engineers World Congress 2007, November 2-7, Bangalore, India

[17] Herfjord, K., Larsen, C.M., Furnes, G., Holmås, T., Randa, K., 1999. *FSI-Simulation of Vortex-Induced Vibrations of Offshore Structures*, Trondheim, Tapir

[18] Hofstede, E., Kottapalli, S., Shams, A., 2017. *Numerical prediction of flow induced vibrations in nuclear reactor applications*, Nuclear Engineering and Design 319, 81–90

[19] Hsiao, F.B., Pan, J.Y., Chiang, C.H., 1992. *The study of vortex shedding frequencies behind tapered circular cylinders*, FED/vol. 138/PVPvol. 245, Symposium on Flow-Induced Vibration and Noise, ASME, vol. 6, 1992, pp. 103-112.

[20] Izhar, A., Qureshi, A.H., Knushnood, S., 2017. *Simulation of Vortex-Induced Vibrations of A Cylinder Using ANSYS CFX Rigid Body Solver*, China Ocean Engineering, Vol. 31, No. 1, 79-90

[21] Kaneko, S., Nakamura, T., Inada, F., Kato, M., Ishihara, K., Nishihara, T., Mureithi, N.W., Langthjem M.A., 2013. *Flow-Induced Vibrations Classifications and Lessons from Practical Experiences*, 2nd edition, Academic Press.

[22] Kinaci, O.K., Lakka, S., Sun, H., Bernitsas, M.M., 2016. *Effect of tip-flow on vortex induced vibration of cylinders for* $Re < 1.2 * 10^5$, Ocean Engineering 117, 130-142

[23] Kondo, N., 2012. *Three-dimensional computation for flow-induced vibrations in in-line and cross-flow directions of a circular cylinder*, Int. J. Numer. Meth. Fluids 2012; 70:158-185

[24] Langen, I., Sigbjørnsen, R., 1979. *Dynamisk Analyse av Konstruksjoner*, Tapir Publishers, Trondheim.

[25] Litteaur, R., McDermott, R., 2017. *CFD Analysis of DHTW*^{TM} *utilizing VE Technology® A Helix Thermowell Design White Paper*, DTC-WP-1003 Rev B, Daily Thermetrics Corp. Houston, TX USA.

[26] Narasimhamurthy, V.D., Andersson, H.I., Pettersen, B., 2009. *Cellular vortex shedding behind a tapered circular cylinder*, Phys. Fluids 21, 044106; https://doi.org/10.1063/1.3103882

[27] Norberg, C., *Flow Around a Circular Cylinder: Aspects of Fluctuating Lift*, Journal of Fluids and Structures (2001) 15, 459 - 469 doi:10.1006/js.2000.0367

[28] Ong, M.C., Utnes, T., Holmedal, L.E., Myrhaug, D., Pettersen, B., 2009. *Numerical simulation of flow around a smooth circular cylinder at very high Reynolds numbers*, Marine Structures 22, 142-153

[29] Panton, R.L., 2013. *Incompressible Flow*, Forth Edition, John Wiley & Sons, Inc., Hoboken, New Jersey

[30] Parnaudeau, P., Heitz, D., Lamballais E., Silvestrini, J.-H., 2007, *Direct numerical simulations of vortex shedding behind cylinders with spanwise linear nonuniformity*, Journal of Turbulence, 8, N13, DOI: 10.1080/14685240600767706

[31] Raja, R.S., 2012. *Coupled fluid structure interaction analysis on a cylinder exposed to ocean wave loading*, Chalmers University of Technology Göteborg.

[32] Salim, S.M., Cheah, S.C., 2009. *Wall y+ strategy for dealing with wall-bounded turbulent flows*, Proc. Int. Multi-Conference Eng Comp Sci 2009 (IMECS 2009), Vol II.

[33] Santos, M.L., Pfeil, M.S., Coutinho, A.L.G.A., (2017). *Vortex shedding by LES 3D numerical simulation*, DOI: 10.20906/CPS/CILAMCE2017-0785.

[34] Schmidt, L.V., 1966. *Fluctuating Force Measurements Upon a Circular Cylinder at Reynolds Numbers up to 5 X* 10^6, Wind Load Problems in Relation to Launch Vehicles, June 7-8, 1966.

[35] Tengs, E., Charrassier, F., Holst, M., Storli, P.T., 2019. *Model Order Reduction Technique Applied on Harmonic Analysis of a Submerged Vibrating Blade*, Int. J. of Applied Mechanics and Engineering, 2019, vol.24, No.1, pp.131-142, DOI: 10.2478/ijame-2019-0009

[36] Upnere, S., 2018. *Numerical study of flow-induced vibrations of mutiple flexibly-mounted cylinders in triangular array*, Latvian Journal of Physics and Technical Sciences 5, 43-52

[37] Wang. E., Xiao, Q., Incecik, A., 2017. *Three-dimensional numerical simulation of two-degree-of-freedom VIV of a circular cylinder with varying natural frequency ratios at Re = 500*, Journal of Fluids and Structures 73 (2017) 162-182

[38] Zienkiewicz, O., Taylor, R., Nithiarasu, P. (7th Ed.) (2013). *The Finite Element Method for Fluid Dynamics*, Elsevier Ltd.

A Analytical Modal Analysis

Assuming that the thermowell can be modeled as a simple cantilevered beam the analytical solution of the natural frequencies is given as:

$$f_n = k_n^2 \sqrt{\frac{EI}{A\rho_s L^4}} \tag{19}$$

where k_n is a constant related to the given mode shape defined as 1.875 for the first mode, L is the beam length, E is the Young's modulus, I is the area moment of inertia and, A is the cross sectional area and ρ_s is the structural density. For a simple cantilevered rod with a diameter of 27.5 mm the first natural frequency is calculated to be 230 Hz.

B Supplementary Plots

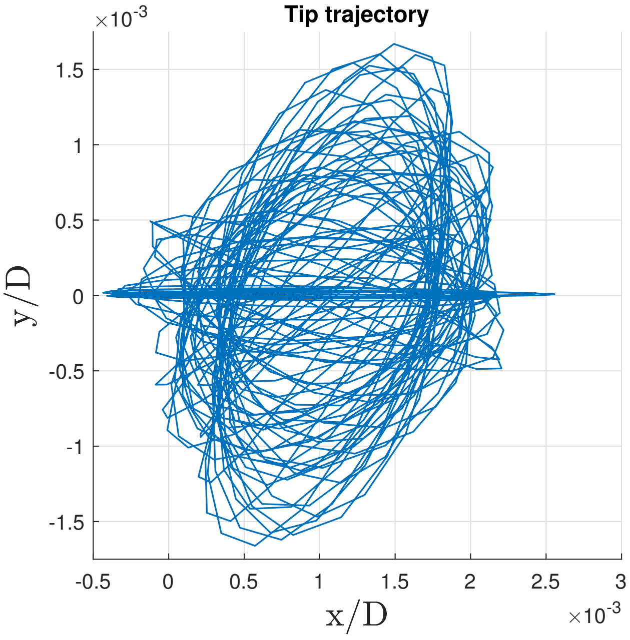

Figure 36: Tip position. FSI case for 19m/s.

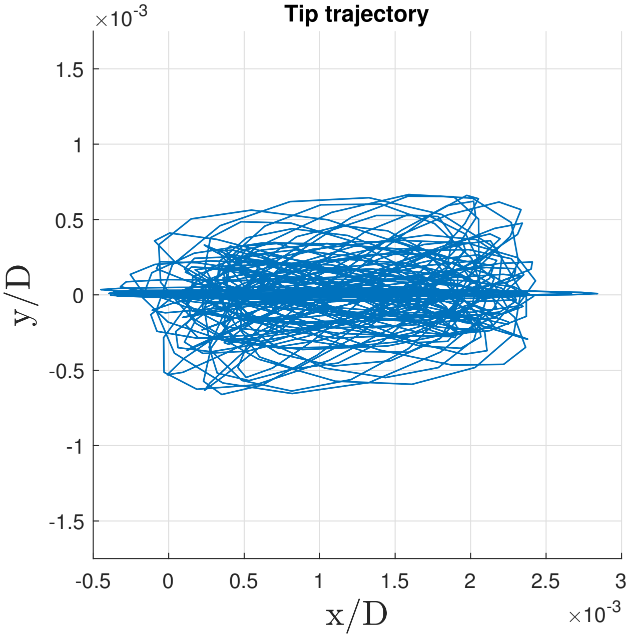

Figure 37: Tip position. FSI case for 20m/s.

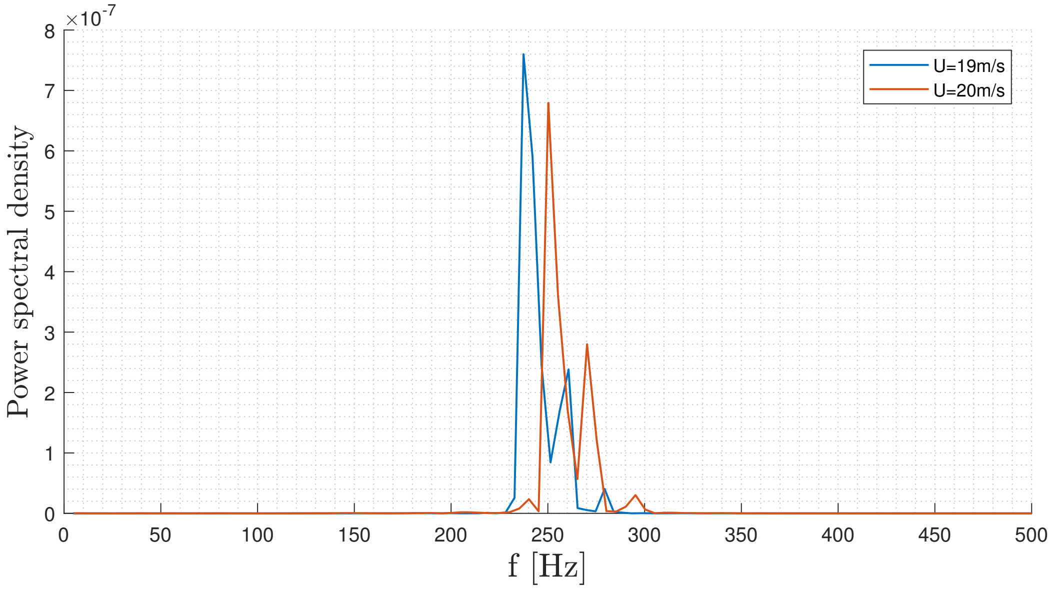

Figure 38: Fast Fourier Transform of the shedding frequency.

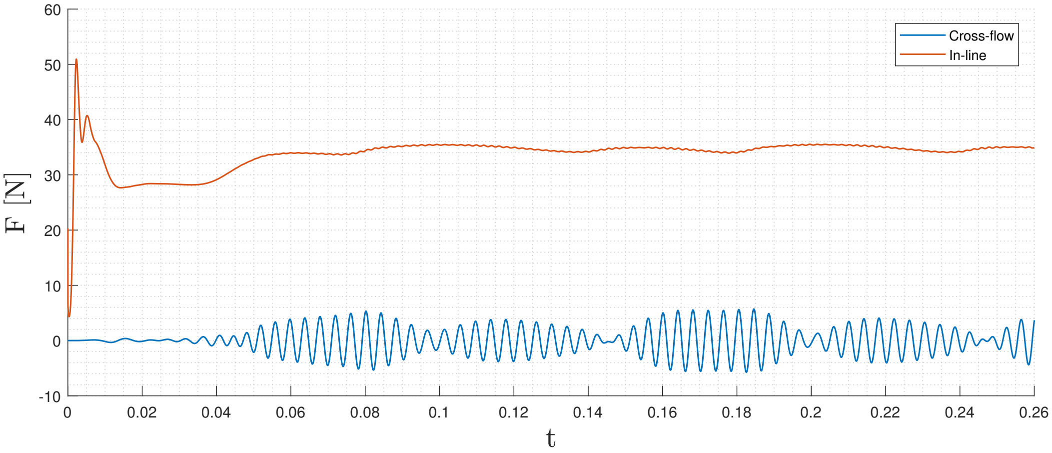

Figure 39: Fluid forces in the FSI case with 19m/s inlet flow.

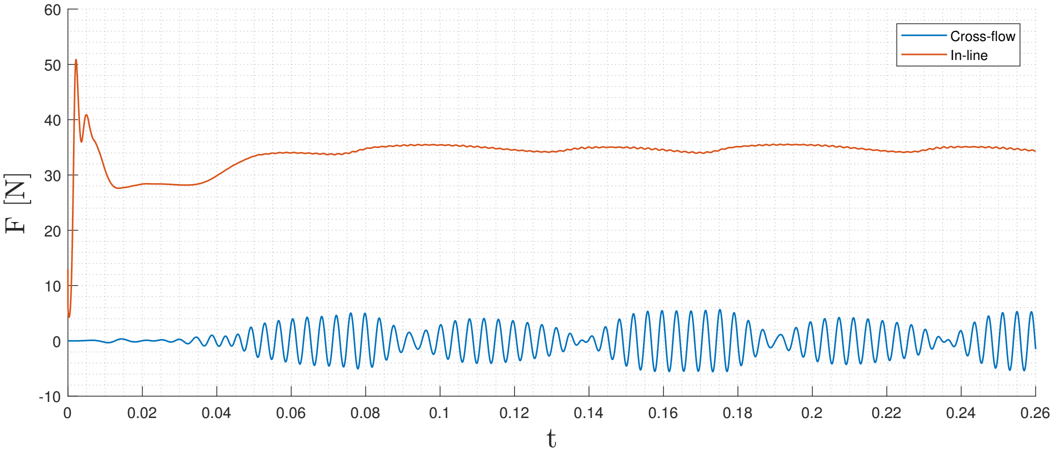

Figure 40: Fluid forces in the FSI case with 20m/s inlet flow.

C Solver Settings Fluent

```
Fluent
Version: 3d, dp, pbns, rke, transient (3d, double precision, pressure-based, realizable
Release: 19.0.0
Title:

Models
------

   Model                        Settings
   -----------------------------------------------------------------
   Space                        3D
   Time                         Unsteady, Bounded 2nd-Order Implicit
   Viscous                      Realizable k-epsilon turbulence model
   Wall Treatment               Enhanced Wall Treatment
   Heat Transfer                Disabled
   Solidification and Melting   Disabled
   Species                      Disabled
   Coupled Dispersed Phase      Disabled
   NOx Pollutants               Disabled
   SOx Pollutants               Disabled
   Soot                         Disabled
   Mercury Pollutants           Disabled

Material Properties
-------------------

   Material: ng (fluid)

      Property                        Units     Method     Value(s)
      -------------------------------------------------------------
      Density                         kg/m3     constant   80
      Cp (Specific Heat)              j/kg-k    constant   1006.43
      Thermal Conductivity            w/m-k     constant   0.0242
      Viscosity                       kg/m-s    constant   4.4e-05
      Molecular Weight                kg/kmol   constant   28.966
      Thermal Expansion Coefficient   1/k       constant   0
      Speed of Sound                  m/s       none       #f

   Material: aluminum (solid)
```

```
      Property               Units    Method     Value(s)
      ---------------------------------------------------
      Density                kg/m3    constant   2719
      Cp (Specific Heat)     j/kg-k   constant   871
      Thermal Conductivity   w/m-k    constant   202.4

Cell Zone Conditions
--------------------

   Zones

      name              id   type
      ----------------------------
      sys-fluid         5    fluid
      sys-fluid_right   4    fluid

   Setup Conditions

      sys-fluid

         Condition       Value
         ---------------------
         Frame Motion?   no
         Mesh Motion?    no

      sys-fluid_right

         Condition       Value
         ---------------------
         Frame Motion?   no
         Mesh Motion?    no

Boundary Conditions
-------------------

   Zones

      name                       id   type
      -----------------------------------------------
      inlet                      8    velocity-inlet
      outlet                     9    pressure-outlet
```

```
      symmetry-sys-fluid         11   symmetry
      symmetry-sys-fluid_right   10   symmetry
      cylinder                   12   wall

   Setup Conditions

      inlet

         Condition                        Value
         -----------------------------------------
         Velocity Magnitude (m/s)         20
         Turbulent Specification Method   1
         Turbulent Intensity (%)          0.8
         Turbulent Length Scale (m)       0.000135

      outlet

         Condition   Value
         -----------------

      symmetry-sys-fluid

         Condition   Value
         -----------------

      symmetry-sys-fluid_right

         Condition   Value
         -----------------

      cylinder

         Condition                  Value
         --------------------------------
         Wall Motion                0
         Shear Boundary Condition   0

Solver Settings
---------------

   Equations
```

```
   Equation     Solved
   -------------------
   Flow         yes
   Turbulence   yes

Numerics

   Numeric                         Enabled
   ---------------------------------------
   Absolute Velocity Formulation   yes

Unsteady Calculation Parameters


   -------------------------------------
   Time Step (s)                   1e-06
   Max. Iterations Per Time Step   11

Relaxation

   Variable                     Relaxation Factor
   ----------------------------------------------
   Pressure                     1
   Density                      1
   Body Forces                  1
   Momentum                     1
   Turbulent Kinetic Energy     1
   Turbulent Dissipation Rate   1
   Turbulent Viscosity          1

Linear Solver

                                Solver     Termination   Residual Reduction
   Variable                     Type       Criterion     Tolerance
   ------------------------------------------------------------------------
   Pressure                     V-Cycle    0.1
   X-Momentum                   Flexible   0.1           0.7
   Y-Momentum                   Flexible   0.1           0.7
   Z-Momentum                   Flexible   0.1           0.7
   Turbulent Kinetic Energy     Flexible   0.1           0.7
   Turbulent Dissipation Rate   Flexible   0.1           0.7
```

```
Pressure-Velocity Coupling

   Parameter                     Value
   -----------------------------------
   Type                          PISO
   Skewness-Neighbour Coupling   yes
   Skewness Correction           1
   Neighbour Correction          1

Discretization Scheme

   Variable                     Scheme
   ------------------------------------------------
   Pressure                     Second Order
   Momentum                     Second Order Upwind
   Turbulent Kinetic Energy     Second Order Upwind
   Turbulent Dissipation Rate   Second Order Upwind

Solution Limits

   Quantity                         Limit
   ---------------------------------------
   Minimum Absolute Pressure        1
   Maximum Absolute Pressure        5e+10
   Minimum Temperature              1
   Maximum Temperature              5000
   Minimum Turb. Kinetic Energy     1e-14
   Minimum Turb. Dissipation Rate   1e-20
   Maximum Turb. Viscosity Ratio    100000
```

D Solver Settings Mechanical

Project

First Saved	Tuesday, April 16, 2019
Last Saved	Saturday, June 8, 2019
Product Version	19.2 Release
Save Project Before Solution	No
Save Project After Solution	No

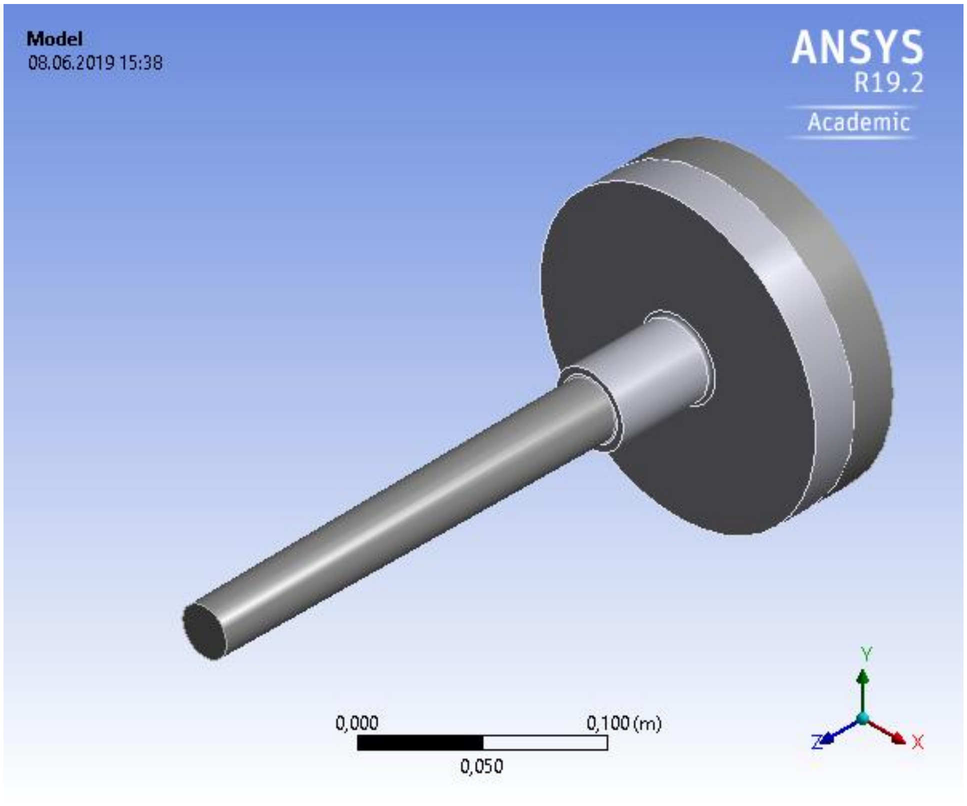

Contents

Units

TABLE 1

Unit System	Metric (m, kg, N, s, V, A) Degrees rad/s Celsius
Angle	Degrees
Rotational Velocity	rad/s
Temperature	Celsius

Model (B4)

Geometry

TABLE 2
Model (B4) > Geometry

Object Name	*Geometry*
State	Fully Defined
Definition	
Source	D:\GAS_FLOW\case_20_files\dp0\SYS\DM\SYS.scdoc
Type	SpaceClaim
Length Unit	Meters
Element Control	Program Controlled
Display Style	Body Color
Bounding Box	
Length X	0,81 m
Length Y	0,42 m

Length Z	0,312 m
Properties	
Volume	1,0064e-003 m³
Mass	7,9002 kg
Scale Factor Value	1,
Statistics	
Bodies	6
Active Bodies	2
Nodes	201479
Elements	138157
Mesh Metric	Element Quality
Min	0,255388460544134
Max	0,999980113232199
Average	0,834907232362342
Standard Deviation	9,77990784502992E-02
Update Options	
Assign Default Material	No
Basic Geometry Options	
Solid Bodies	Yes
Surface Bodies	Yes
Line Bodies	Yes
Parameters	Independent
Parameter Key	
Attributes	Yes
Attribute Key	
Named Selections	Yes
Named Selection Key	
Material Properties	Yes
Advanced Geometry Options	
Use Associativity	Yes
Coordinate Systems	Yes
Coordinate System Key	
Reader Mode Saves Updated File	No
Use Instances	Yes
Smart CAD Update	Yes
Compare Parts On Update	No
Analysis Type	3-D
Mixed Import Resolution	None
Clean Bodies On Import	No
Stitch Surfaces On Import	No
Decompose Disjoint Geometry	Yes
Enclosure and Symmetry Processing	Yes

TABLE 3
Model (B4) > Geometry > Body Groups

Object Name	*SYS*
State	Meshed
Graphics Properties	
Visible	Yes
Definition	
Suppressed	No
Assignment	Structural Steel

Coordinate System	Default Coordinate System
Bounding Box	
Length X	0,81 m
Length Y	0,42 m
Length Z	0,312 m
Properties	
Volume	1,0064e-003 m³
Mass	7,9002 kg
Centroid X	-1,6251e-010 m
Centroid Y	-2,2046e-018 m
Centroid Z	4,4819e-002 m
Moment of Inertia Ip1	3,9869e-002 kg·m²
Moment of Inertia Ip2	3,9869e-002 kg·m²
Moment of Inertia Ip3	2,0031e-002 kg·m²
Statistics	
Nodes	201479
Elements	138157
Mesh Metric	Element Quality
Min	0,255388460544134
Max	0,999980113232199
Average	0,834907232362342
Standard Deviation	9,77990784502992E-02
CAD Attributes	
PartTolerance:	0,00000001
Color:143.168.175	
Color:143.175.143	

TABLE 4
Model (B4) > Geometry > SYS > Parts

Object Name	*Fluid Right*	*Fluid*	*Surface*	*Surface*	*thermowell*	*small_bore*
State	Suppressed				Meshed	
Graphics Properties						
Visible	No				Yes	
Transparency					1	
Definition						
Suppressed	Yes				No	
Stiffness Behavior	Flexible					
Coordinate System	Default Coordinate System					
Reference Temperature	By Environment					
Behavior	None					
Thickness			0, m			
Thickness Mode			Refresh on Update			
Offset Type			Middle			
Material						
Assignment	Structural Steel					
Nonlinear Effects	Yes					

<table>
<tr><td>Thermal Strain Effects</td><td colspan="6">Yes</td></tr>
<tr><th colspan="7">Bounding Box</th></tr>
<tr><td>Length X</td><td>0,21 m</td><td>0,81 m</td><td colspan="2">9,25e-002 m</td><td colspan="2">0,156 m</td></tr>
<tr><td>Length Y</td><td>0,21 m</td><td>0,42 m</td><td colspan="2">0, m</td><td colspan="2">0,156 m</td></tr>
<tr><td>Length Z</td><td colspan="2">0,218 m</td><td colspan="2">0,29 m</td><td>0,312 m</td><td>7,2e-002 m</td></tr>
<tr><th colspan="7">Properties</th></tr>
<tr><td>Volume</td><td>7,4268e-003 m^3</td><td>6,6613e-002 m^3</td><td colspan="2">0, m^3</td><td>5,8363e-004 m^3</td><td>4,2276e-004 m^3</td></tr>
<tr><td>Mass</td><td>58,3 kg</td><td>522,91 kg</td><td colspan="2"></td><td>4,5815 kg</td><td>3,3187 kg</td></tr>
<tr><td>Centroid X</td><td>-4,5824e-019 m</td><td>0,21694 m</td><td>-5,9372e-002 m</td><td>5,9372e-002 m</td><td>8,7206e-018 m</td><td>-3,8686e-010 m</td></tr>
<tr><td>Centroid Y</td><td>-1,833e-018 m</td><td>-4,2692e-018 m</td><td colspan="2">0, m</td><td>-2,7258e-018 m</td><td>-1,4851e-018 m</td></tr>
<tr><td>Centroid Z</td><td>0,20308 m</td><td>0,203 m</td><td colspan="2">0,16766 m</td><td>5,2213e-002 m</td><td>3,4611e-002 m</td></tr>
<tr><td>Moment of Inertia Ip1</td><td>0,3917 kg·m^2</td><td>10,469 kg·m^2</td><td colspan="2">0, kg·m^2</td><td>3,3936e-002 kg·m^2</td><td>5,3359e-003 kg·m^2</td></tr>
<tr><td>Moment of Inertia Ip2</td><td>0,3917 kg·m^2</td><td>31,252 kg·m^2</td><td colspan="2">0, kg·m^2</td><td>3,3936e-002 kg·m^2</td><td>5,3359e-003 kg·m^2</td></tr>
<tr><td>Moment of Inertia Ip3</td><td>0,32369 kg·m^2</td><td>37,576 kg·m^2</td><td colspan="2">0, kg·m^2</td><td>1,004e-002 kg·m^2</td><td>9,9914e-003 kg·m^2</td></tr>
<tr><td>Surface Area(approx.)</td><td colspan="2"></td><td colspan="2">5,2925e-002 m^2</td><td colspan="2"></td></tr>
<tr><th colspan="7">Statistics</th></tr>
<tr><td>Nodes</td><td colspan="4">0</td><td>125314</td><td>76165</td></tr>
<tr><td>Elements</td><td colspan="4">0</td><td>86919</td><td>51238</td></tr>
<tr><td>Mesh Metric</td><td colspan="6">Element Quality</td></tr>
<tr><td>Min</td><td colspan="4">0</td><td>0,255388460544134</td><td>0,316412982165642</td></tr>
<tr><td>Max</td><td colspan="4">0</td><td>0,999980113232199</td><td>0,999701795298631</td></tr>
<tr><td>Average</td><td colspan="4">0</td><td>0,837580323676618</td><td>0,830372659897657</td></tr>
<tr><td>Standard Deviation</td><td colspan="4">0</td><td>9,82594266751167E-02</td><td>9,68455161613117E-02</td></tr>
</table>

Coordinate Systems

TABLE 5
Model (B4) > Coordinate Systems > Coordinate System

Object Name	*Global Coordinate System*
State	Fully Defined
Definition	
Type	Cartesian
Coordinate System ID	0,
Origin	
Origin X	0, m
Origin Y	0, m
Origin Z	0, m
Directional Vectors	
X Axis Data	[1, 0, 0,]
Y Axis Data	[0, 1, 0,]
Z Axis Data	[0, 0, 1,]

Connections

TABLE 6
Model (B4) > Connections

Object Name	*Connections*
State	Fully Defined
Auto Detection	
Generate Automatic Connection On Refresh	Yes
Transparency	
Enabled	Yes

TABLE 7
Model (B4) > Connections > Contacts

Object Name	*Contacts*
State	Fully Defined
Definition	
Connection Type	Contact
Scope	
Scoping Method	Geometry Selection
Geometry	All Bodies
Auto Detection	
Tolerance Type	Slider
Tolerance Slider	0,
Tolerance Value	2,4107e-003 m
Use Range	No
Face/Face	Yes
Face Overlap Tolerance	Off
Cylindrical Faces	Include
Face/Edge	No
Edge/Edge	No
Priority	Include All
Group By	Bodies
Search Across	Bodies
Statistics	
Connections	1
Active Connections	1

TABLE 8
Model (B4) > Connections > Contacts > Contact Regions

Object Name	*Bonded - thermowell To small_bore*
State	Fully Defined
Scope	
Scoping Method	Geometry Selection
Contact	1 Face
Target	1 Face
Contact Bodies	thermowell
Target Bodies	small_bore
Protected	No
Definition	
Type	Bonded
Scope Mode	Manual
Behavior	Program Controlled
Trim Contact	Program Controlled

Suppressed	No
Advanced	
Formulation	MPC
Detection Method	Program Controlled
Constraint Type	Program Controlled
Pinball Region	Program Controlled
Geometric Modification	
Contact Geometry Correction	None
Target Geometry Correction	None

Mesh

TABLE 9
Model (B4) > Mesh

Object Name	*Mesh*
State	Solved
Display	
Display Style	Use Geometry Setting
Defaults	
Physics Preference	Mechanical
Solver Preference	Mechanical APDL
Element Order	Program Controlled
Element Size	1,906e-002 m
Sizing	
Use Adaptive Sizing	No
Growth Rate	1,1725
Max Size	4,8212e-002 m
Mesh Defeaturing	Yes
Defeature Size	Default (9,53e-005 m)
Capture Curvature	No
Capture Proximity	Yes
Proximity Min Size	Default (1,906e-004 m)
Num Cells Across Gap	2
Proximity Size Function Sources	Faces and Edges
Bounding Box Diagonal	0,96428 m
Average Surface Area	4,7613e-002 m^2
Minimum Edge Length	2,042e-002 m
Quality	
Check Mesh Quality	Yes, Errors
Error Limits	Standard Mechanical
Target Quality	Default (0.050000)
Smoothing	High
Mesh Metric	Element Quality
Min	0,25539
Max	0,99998
Average	0,83491
Standard Deviation	9,7799e-002
Inflation	
Use Automatic Inflation	None
Inflation Option	Smooth Transition
Transition Ratio	0,272
Maximum Layers	5

Growth Rate	1,2
Inflation Algorithm	Pre
View Advanced Options	No
Advanced	
Number of CPUs for Parallel Part Meshing	Program Controlled
Straight Sided Elements	No
Rigid Body Behavior	Dimensionally Reduced
Triangle Surface Mesher	Program Controlled
Topology Checking	Yes
Pinch Tolerance	Default (1,7154e-004 m)
Generate Pinch on Refresh	No
Sheet Loop Removal	No
Statistics	
Nodes	201479
Elements	138157

TABLE 10
Model (B4) > Mesh > Mesh Controls

Object Name	*Edge Sizing*	*Face Sizing*	*Face Sizing 2*	*Edge Sizing 2*
State	Suppressed	Fully Defined	Suppressed	Fully Defined
Scope				
Scoping Method	Geometry Selection			
Geometry	No Selection	2 Faces	1 Face	2 Edges
Definition				
Suppressed	Yes	No	Yes	No
Active	No, Suppressed		No, Suppressed	
Type	Number of Divisions	Element Size		Number of Divisions
Number of Divisions	30			83
Element Size		3,25e-003 m	5,e-005 m	
Advanced				
Defeature Size	Default (9,53e-005 m)		Default (2,5e-005 m)	
Behavior	Hard		Soft	Hard
Capture Curvature	No			
Capture Proximity	No			
Growth Rate			Default (1,1725)	
Bias Type				No Bias

Transient (B5)

TABLE 11
Model (B4) > Analysis

Object Name	*Transient (B5)*
State	Solved
Definition	
Physics Type	Structural
Analysis Type	Transient
Solver Target	Mechanical APDL
Options	
Environment Temperature	22, °C
Generate Input Only	No

TABLE 12
Model (B4) > Transient (B5) > Initial Conditions

Object Name	*Initial Conditions*
State	Fully Defined

TABLE 13
Model (B4) > Transient (B5) > Initial Conditions > Initial Condition

Object Name	*Modal (None)*
State	Fully Defined
Definition	
Modal Environment	None Available
Pre-Stress Environment	None

TABLE 14
Model (B4) > Transient (B5) > Analysis Settings

Object Name	*Analysis Settings*
State	Fully Defined
Restart Analysis	
Restart Type	Program Controlled
Status	Done
Step Controls	
Number Of Steps	1,
Current Step Number	1,
Step End Time	1, s
Auto Time Stepping	Off
Define By	Substeps
Number Of Substeps	1,
Time Integration	On
Solver Controls	
Solver Type	Program Controlled
Weak Springs	Off
Large Deflection	Off
Restart Controls	
Generate Restart Points	Program Controlled
Retain Files After Full Solve	Yes
Combine Restart Files	Yes
Nonlinear Controls	
Newton-Raphson Option	Program Controlled
Force Convergence	Program Controlled
Moment Convergence	Program Controlled
Displacement Convergence	Program Controlled
Rotation Convergence	Program Controlled
Line Search	Program Controlled
Stabilization	Off
Output Controls	
Stress	Yes
Strain	No
Nodal Forces	No
Contact Miscellaneous	No
General Miscellaneous	No
Store Results At	Specified Recurrence Rate
--- Value	20,
Damping Controls	

Stiffness Coefficient Define By	Direct Input
Stiffness Coefficient	0,
Mass Coefficient	0,
Numerical Damping	Program Controlled
Numerical Damping Value	0,1
Analysis Data Management	
Solver Files Directory	D:\GAS_FLOW\case_20_files\dp0\SYS-1\MECH\
Future Analysis	None
Scratch Solver Files Directory	
Save MAPDL db	No
Contact Summary	Program Controlled
Delete Unneeded Files	Yes
Nonlinear Solution	No
Solver Units	Active System
Solver Unit System	mks

TABLE 15
Model (B4) > Transient (B5) > Loads

Object Name	*Fixed Support*	*Fluid Solid Interface*
State	Fully Defined	
Scope		
Scoping Method	Geometry Selection	
Geometry	1 Face	
Definition		
Type	Fixed Support	Fluid Solid Interface
Suppressed	No	
Interface Number		1,
Data to Transfer [Expert]		Program Controlled

Solution (B6)

TABLE 16
Model (B4) > Transient (B5) > Solution

Object Name	*Solution (B6)*
State	Solved
Adaptive Mesh Refinement	
Max Refinement Loops	1,
Refinement Depth	2,
Information	
Status	Done
MAPDL Elapsed Time	49 h 3 m
MAPDL Memory Used	1,3154 GB
MAPDL Result File Size	60,002 GB
Post Processing	
Beam Section Results	No

TABLE 17
Model (B4) > Transient (B5) > Solution (B6) > Solution Information

Object Name	*Solution Information*
State	Solved
Solution Information	
Solution Output	Solver Output
Newton-Raphson Residuals	0

Identify Element Violations	0
Update Interval	2,5 s
Display Points	All
FE Connection Visibility	
Activate Visibility	Yes
Display	All FE Connectors
Draw Connections Attached To	All Nodes
Line Color	Connection Type
Visible on Results	No
Line Thickness	Single
Display Type	Lines

Material Data

Structural Steel

TABLE 18
Structural Steel > Constants

Density	7850, kg m^-3
Isotropic Secant Coefficient of Thermal Expansion	1,2e-005 C^-1
Specific Heat Constant Pressure	434, J kg^-1 C^-1
Isotropic Thermal Conductivity	60,5 W m^-1 C^-1
Isotropic Resistivity	1,7e-007 ohm m

TABLE 19
Structural Steel > Color

Red	Green	Blue
132,	139,	179,

TABLE 20
Structural Steel > Compressive Ultimate Strength

Compressive Ultimate Strength Pa
0,

TABLE 21
Structural Steel > Compressive Yield Strength

Compressive Yield Strength Pa
2,5e+008

TABLE 22
Structural Steel > Tensile Yield Strength

Tensile Yield Strength Pa
2,5e+008

TABLE 23
Structural Steel > Tensile Ultimate Strength

Tensile Ultimate Strength Pa
4,6e+008

TABLE 24
Structural Steel > Isotropic Secant Coefficient of Thermal Expansion

Zero-Thermal-Strain Reference Temperature C
22,

TABLE 25
Structural Steel > Alternating Stress Mean Stress

Alternating Stress Pa	Cycles	Mean Stress Pa
3,999e+009	10,	0,
2,827e+009	20,	0,
1,896e+009	50,	0,
1,413e+009	100,	0,
1,069e+009	200,	0,
4,41e+008	2000,	0,
2,62e+008	10000	0,
2,14e+008	20000	0,
1,38e+008	1,e+005	0,
1,14e+008	2,e+005	0,
8,62e+007	1,e+006	0,

TABLE 26
Structural Steel > Strain-Life Parameters

Strength Coefficient Pa	Strength Exponent	Ductility Coefficient	Ductility Exponent	Cyclic Strength Coefficient Pa	Cyclic Strain Hardening Exponent
9,2e+008	-0,106	0,213	-0,47	1,e+009	0,2

TABLE 27
Structural Steel > Isotropic Elasticity

Young's Modulus Pa	Poisson's Ratio	Bulk Modulus Pa	Shear Modulus Pa	Temperature C
2,e+011	0,3	1,6667e+011	7,6923e+010	

TABLE 28
Structural Steel > Isotropic Relative Permeability

Relative Permeability
10000

TABLE 29
Structural Steel > Damping Factor (?)

Mass-Matrix Damping Multiplier
0,

TABLE 30
Structural Steel > Damping Factor (?)

k-Matrix Damping Multiplier
1,2058e-006

NTNU
Norwegian University of
Science and Technology

DNV·GL